Volume 4
Number 13
7 July 2023
Pages 2687–2876

Materials Advances

rsc.li/materials-advances

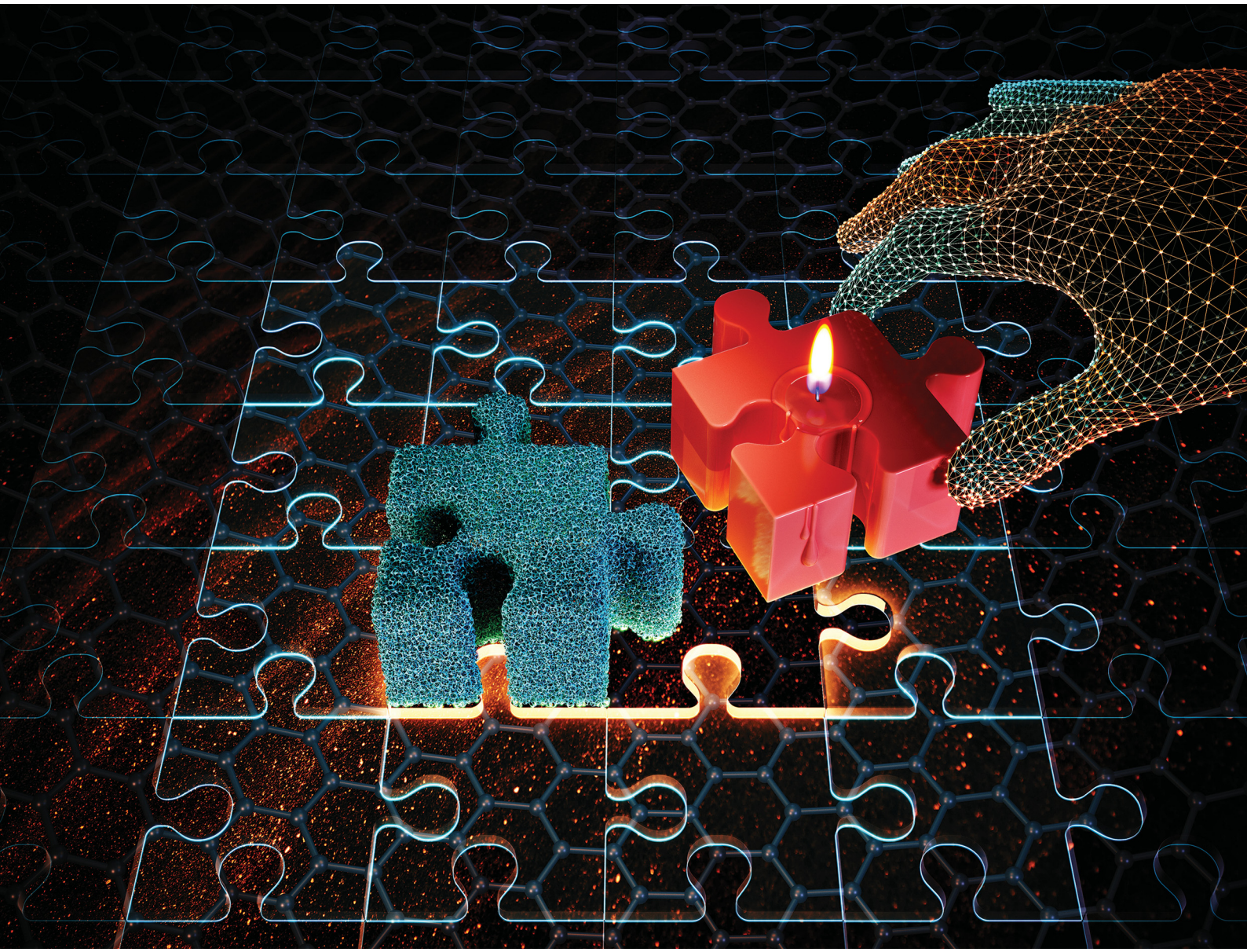

ISSN 2633-5409

ROYAL SOCIETY OF CHEMISTRY

REVIEW ARTICLE

Ahmadreza Ghaffarkhah, Mohammad Arjmand *et al.*
2D nanomaterial aerogels integrated with phase change materials: a comprehensive review

Materials Advances

ROYAL SOCIETY OF CHEMISTRY

REVIEW

View Article Online
View Journal | View Issue

Cite this: *Mater. Adv.*, 2023, 4, 2698

2D nanomaterial aerogels integrated with phase change materials: a comprehensive review

Sara Rostami, Ahmadreza Ghaffarkhah,* Ali Akbar Isari, Seyyed Alireza Hashemi and Mohammad Arjmand *

Aerogels of 2D nanomaterials are considered ideal platforms for encapsulating phase change materials (PCMs) due to their unique properties, including their light weight, high porosity, large specific surface area, adjustable thermal/electrical conductivity, and mechanical flexibility, which allows for rationalizing phase transformation behaviors. The combination of these versatile aerogels and PCMs is a significant milestone in pioneering advanced composite PCMs, where multifunctionality and low cost are of utmost importance. This review provides a systematic overview of the state-of-the-art advances in 2D nanomaterial-based aerogel fabrication, including drying approaches and pre-treatment methods, as well as their potential uses in composite PCMs. It also highlights the versatile roles of different aerogels in composite PCMs and the relationships between their inherent characteristics and functionalities. This review mainly aims to increase interest in interdisciplinary research and provide guidance for the rational design of advanced multifunctional 2D aerogel-based composite PCMs, thus facilitating significant breakthroughs in both fundamental research and commercial applications.

Received 27th January 2023,
Accepted 1st May 2023

DOI: 10.1039/d3ma00049d

rsc.li/materials-advances

1. Introduction

The impact of environmental concerns on human life is widespread, with the consumption of fossil fuels being a major contributor to climate change, resulting in many environmental challenges.[1–4] In recent years, energy management has been advanced to address these issues by implementing sustainable, low-cost energy sources. One important aspect of this effort is thermal energy storage, which plays a vital role in the prevalent adoption of renewable energy sources. Phase change materials (PCMs) are a crucial component of thermal energy management, as they can absorb and release large amounts of heat during phase transitions, rendering them well-suited for a wide range of industrial and residential applications.[5–9] Depending on the specific conditions, these so-called "smart energy management materials" can store energy through melting/solidifying and

Nanomaterials and Polymer Nanocomposites Laboratory, School of Engineering, University of British Columbia, Kelowna, BC, V1V 1V7, Canada.
E-mail: ah.ghaffarkhah@ubc.ca, mohammad.arjmand@ubc.ca

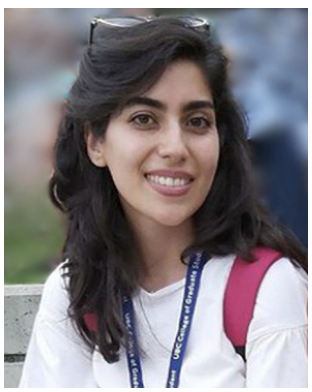

Sara Rostami

Sara Rostami is currently serving as a Visiting International Research Student (VIRS) at the School of Engineering, University of British Columbia, Okanagan Campus. She is working under the guidance of Dr Mohammad Arjmand, and her research mainly centers on thermal management systems, PCMs, and nanomaterials. Furthermore, Sara is also actively involved in exploring the domains of 3D printing and liquid-in-liquid printing of hydrogels and inks based on 2D nanomaterials.

Ahmadreza Ghaffarkhah

Ahmadreza Ghaffarkhah is a PhD candidate in the School of Engineering at the University of British Columbia, Okanagan Campus. His research interests include the synthesis of carbon-based nanomaterials and MOFs, polymer processing and forming, and intrinsically conductive polymers. Additionally, he works on 3D printing and liquid-in-liquid printing of carbon-based hydrogels and inks. Google scholar: ***https://scholar.google.com/citations?user=bZSCwa4AAAAJ&hl=en.***

release it with a minimal loss.[10–13] PCMs can be classified into solid–gas, liquid–gas, solid–solid, and solid–liquid systems based on the type of phase transition.[6,14,15] Amongst all, solid–liquid PCMs have shown promise due to their higher phase change enthalpies and less volume change compared to solid–solid and liquid/solid–gas systems, respectively.[16–19]

Solid–liquid PCMs are broadly divided into two subcategories: inorganic and organic.[20] Inorganic PCMs, like hydrated salts, salts, and metals, possess high volumetric latent heat and storage capacity, but they may suffer from issues such as high density, chemical instability, and low availability.[21] Organic PCMs, such as paraffin, alcohols, and fatty acids, exhibit characteristics like congruent melting, self-nucleation, and non-corrosiveness, which allow them to be used in a wide range of practical applications.[22,23] However, they may have drawbacks such as low thermal conductivity and liquid phase leakage, hindering far-ranging applications of PCMs.[24–26] These challenges are addressed in recent studies by incorporating thermally conductive micro-to-nano additives, such as carbons, metals, and metal oxides, to enhance thermal conductivity and improve the performance or to encapsulate PCMs.[11,27–32] In this regard, nanomaterials of the carbon family have been researched extensively due to their exceptional thermal conductivity reaching up to 4000 W m^{-1} K^{-1}.[33,34] For instance, the combination of expanded graphite/cellulose nanofibers (CNFs)/boron nitride (BN) with polyethylene glycol (PEG) 4000 showcased a thermal conductivity of 0.32 W m^{-1} K^{-1}, leading to nearly 3300% enhancement of the thermal conductivity of the pristine PEG.[35]

Another promising approach in thermal energy storage management is the encapsulation of PCMs, which can be achieved through two main methods: microencapsulation and nanoencapsulation.[36–39] Microencapsulation involves enclosing PCMs in a shell made of organic, inorganic, or polymeric materials. On the other hand, nanoencapsulation involves infiltrating PCMs into porous materials such as aerogels. Nanoencapsulation not only improves the thermal conductivity, melting, and solidification rate of PCMs but also enhances their form stability.[40–43] Energy storage reinforcement of form-stable composite PCMs explicitly relies on the structure and properties of the ESI.[44–47] As a cutting-edge concept, aerogels, known as hyper-porous nanostructures, have been proposed as supporting scaffolds to confine PCMs.[48–52] Additionally, the properties of the aerogels used for encapsulation can be integrated into composite PCMs to create multifunctional thermal management systems. For example, by combining conductive aerogels with PCMs, it is possible to achieve both thermal insulation and sensing/electromagnetic interference (EMI) shielding simultaneously.[53–60]

In the field of aerogel-based PCMs, the use of 2D nanomaterials like graphene, MXene, and hexagonal boron nitride (h-BN) has been demonstrated to have exceptional thermal conductivity and high capacity for loading PCMs. These 2D nanomaterial-based aerogels have properties that make them suitable to be used as multifunctional composite PCMs,

Ali Akbar Isari

Aliakbar Isari is a PhD student at the University of British Columbia, Okanagan Campus School of Engineering. He has been working on graphene-based materials for EMI shielding and oil absorption applications. His research interest includes the synthesis of carbon-based nanomaterials, aerogels, photocatalysis, and emulsion printing.

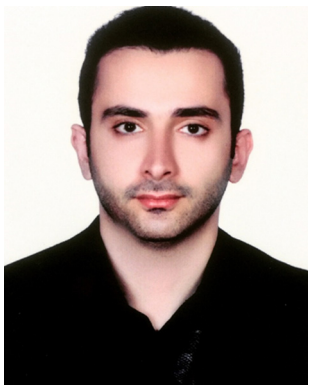

Seyyed Alireza Hashemi

Seyyed Alireza Hashemi is a PhD student of Mechanical Engineering at the University of British Columbia, Okanagan Campus. His research focuses on the design and development of 2D carbonaceous nanomaterials, hybrid aerogels based on interfacial complexation, 3D-printed conductive constructs, advanced electromagnetic shields, and piezoresistive sensors.

Mohammad Arjmand

Dr Mohammad Arjmand is a leading and award-winning researcher in the areas of nanotechnology and polymer science and engineering. Dr Arjmand is an assistant professor (since 2018) at the University of British Columbia, Okanagan campus (UBCO). He is also a Canada Research Chair in Advanced Materials and Polymer Engineering and the technical lead of the Plastic Recycling Research Cluster at UBCO. Dr Arjmand directs Nanomaterials and Polymer Nanocomposites Laboratory (NPNL), which focuses on the synthesis and engineering of multifunctional nanomaterials and polymer nanocomposites. Prior to joining UBCO, Dr Arjmand was a postdoctoral fellow at the Universities of Calgary and Toronto.

e.g., ease of functionalization and surface modification, high electrical conductivity in the case of MXene and graphene, and chemical/mechanical stability in the case of h-BN.[61,62] Due to these favorable characteristics and numerous studies on their fabrication, the future of 2D aerogel-based composite PCMs is looking boundless with many studies to be published in this field.

To date, several review articles have been published on thermal conductivity enhancement, thermal properties, and applications of PCMs and composite PCMs in thermal energy storage.[63–68] However, these works have barely discussed the significant developments in aerogel fabrication and the impact of aerogel structures on the thermophysical performance of corresponding composite PCMs. Additionally, recent advances in multifunctional and mechanically flexible aerogel-based composite PCMs require further evaluation. In this review, our aim is to comprehensively describe the definition of 2D nanomaterials and their fundamental development in multifunctional aerogel fabrication. We will also highlight interdisciplinary research fields that combine aerogels and PCMs. Our focus will center around the general description and characteristics of PCMs (Section 2), state-of-the-art advances in aerogel fabrication, conventional 2D nanomaterials utilized in aerogel fabrication (Section 3), and 2D nanomaterial aerogel-based composite PCMs (Section 4). In Section 5, we will conclude by addressing the current core challenges and future prospects of composite PCMs. Upon completion of this review, readers will gain a better understanding of the most recent developments in aerogel-based composite PCMs, including the significant role played by 2D nanomaterials in this field.

2. An overview of PCMs

2.1. Classification of PCMs

PCMs can absorb or release significant amounts of latent heat during the reversible isothermal phase change process through crystallization or condensation. There are several subcategories of PCMs based on their phase transition, including solid–gas, liquid–gas, solid–solid, and solid–liquid.[69] Among all, solid–solid PCMs, such as polyurethane and polybutadiene, can store heat by modifying their crystalline structure at a well-defined temperature; however, they suffer from low latent heat and volume change. On the other hand, solid/liquid–gas PCMs, which necessitate large volumes and high pressures to store materials in their gas phase, are not commonly used in practical energy storage systems. Therefore, solid–liquid PCMs are deemed the most practical option as they possess high latent heat, stable phase change temperature, and minimal volume change of 10% or less. They are compatible with significant volume changes in thermal energy storage systems, making them a promising option for practical applications. Due to these characteristics, solid–liquid PCMs are suitable for various thermal management applications in diverse fields such as construction, automotive, aerospace, and electronics.[6,15,70]

Solid–liquid PCMs can be classified into three types: organic, inorganic, and eutectic, which is a combination of organic and inorganic PCMs. The unique property of organic PCMs is their ability to undergo congruent melting without phase separation or loss of latent heat. These materials also offer other advantages, including non-corrosiveness, self-nucleation, non-segregation, low supercooling degree, and chemical stability. These features make organic PCMs an attractive choice for various applications, such as thermal energy storage systems and temperature regulation in buildings and vehicles. Nevertheless, organic PCMs also possess several disadvantages, such as flammability, liquid phase leakage, and low thermal conductivity (0.40–0.70 $W\,m^{-1}\,K^{-1}$), which restrict their use in specific applications.[71–74] Thus, there is a current trend in developing PCM composites that overcome the limitations of organic PCMs and expand their scope of applications.

On the other hand, inorganic PCMs are composed of salts, hydrated salts, and metals. These materials have a higher latent heat of fusion per unit volume and, consequently, a higher thermal conductivity compared to organic PCMs. Among all, hydrated salts have limitations such as inconsistent melting, severe phase separation, and supercooling degree, which restrict their widespread use in thermal energy systems. Similarly, metal hydrates and metals, other categories of inorganic PCMs, are not commonly employed due to their relatively high density. Therefore, organic PCMs remain the preferred choice for most practical applications due to their cost-effectiveness and ease of handling.[75–77]

Eutectics, a combination of multiple organic and inorganic PCMs, offer several advantages such as lower melting and freezing points and enhanced thermophysical characteristics.[78] However, It is critical to forecast the points and estimate the concentration of different materials of eutectics to predict their functional properties. Fortunately, numerous experiments have been conducted to predict the density and thermal conductivity of eutectics, and theoretical relations can also be used to predict these parameters.[79,80] Additionally, the fusion latent heat of eutectics can be determined by employing the enthalpy and entropy balance.[81] These findings are essential in expanding the applications of eutectics in thermal management systems, such as those used in buildings and vehicles, and therefore, in the future, these classes of PCMs might be used in large-scale industrial applications.

2.2. General characteristics of PCMs

The effectiveness of PCMs for thermal energy storage and release in various applications is determined by several parameters, including thermal conductivity, melting temperature, freezing temperature, melting latent heat, and freezing latent heat. Among these parameters, thermal conductivity is of utmost importance as it is directly related to the rate at which the material conducts heat, and thus determines how efficiently thermal energy is transferred between the material and its surrounding. Thermal conductivity is expressed in unit of Watts per meter-Kelvin ($W\,m^{-1}\,K^{-1}$), and high thermal conductivity is desirable for fast heat transfer and effective energy storage.[76,82]

Melting temperature is another critical characteristic of a PCM because it determines the temperature range over which the material can store thermal energy. For effective thermal

energy storage, the melting temperature should be within the desired operating temperature range of the system. On the other hand, the freezing temperature is the temperature at which the PCM changes from a liquid to a solid and determines the temperature range over which the material can release thermal energy. For effective thermal energy release, the freezing temperature should be below the desired operating temperature of the system. Both melting and freezing temperatures are expressed in unit of degrees Celsius (°C).

Melting latent heat is the thermal energy required to change the PCM from a solid to a liquid, expressed in unit of Joules per gram (J g^{-1}). It is a critical characteristic of a PCM because it determines the amount of thermal energy that can be stored in the material. A high melting latent heat is desirable for effective thermal energy storage. Similarly, freezing latent heat is the amount of thermal energy released when the material changes from a liquid to a solid, also expressed in units of Joules per gram (J g^{-1}). A high freezing latent heat is desirable for effective thermal energy release.[76,82]

The combination of these parameters not only determines the effectiveness of a PCM for thermal energy storage and release, but also presents exciting opportunities for energy-efficient applications. For instance, PCMs have the potential to revolutionize the building industry by reducing energy consumption for heating and cooling. By incorporating PCMs into building materials such as walls, floors, and roofs, buildings can store thermal energy during the day and release it at night, reducing the need for HVAC systems and ultimately lowering energy costs. As we strive to develop more sustainable and efficient energy solutions, the study and development of PCMs is becoming increasingly important. By understanding and optimizing the characteristics of PCMs, we can unlock their potential for a wide range of applications and contribute to a greener, more energy-efficient future.

2.3. Selection criteria of PCMs

The selection of appropriate PCMs is an important aspect of designing thermal energy storage systems. Several criteria need to be considered when selecting the most suitable PCM for a given application. These criteria include chemical, economic, kinetic, and thermodynamic properties.[76,82]

From a chemical perspective, PCMs must have desirable characteristics such as chemical and physical stability, inflammability, nontoxicity, and non-corrosiveness. The chemical stability of a PCM is important as it ensures that the material does not undergo any unwanted chemical reactions or decompositions during the phase change process, which can affect the system's performance. Physical stability is also crucial, as it ensures that the PCM remains in its intended form, whether solid or liquid, during the phase change process. Inflammability, nontoxicity, and non-corrosiveness are essential characteristics to ensure safety during operation.

Economically, PCMs that are readily available and affordable are preferred. In many cases, the cost of a PCM may be a significant factor in selecting a material, particularly in large-scale applications. Some PCMs that are readily available and affordable include paraffin waxes, fatty acids, and eutectic mixtures.[76,82]

Kinetic properties are also essential to consider when selecting a PCM. High nucleation rates and crystal growth rates are critical to avoid supercooling of the liquid phase and to address heat recovery challenges. The supercooling of a PCM occurs when it remains in a liquid state even though its temperature has dropped below its freezing point. This can cause the PCM to solidify abruptly, leading to potential issues such as expansion and cracking. Therefore, it is important to select PCMs with high nucleation rates to avoid supercooling.

Thermodynamic properties of PCMs are of utmost importance when selecting the most appropriate material. These include operating temperature, latent heat of fusion, thermal conductivity, and thermal stability. The operating temperature is one of the most critical factors in selecting a PCM since it determines the phase change process demands. For example, if a PCM is required for a low-temperature application, paraffin waxes or fatty acids with a melting temperature below 40 °C may be suitable. However, if the application requires a high-temperature PCM, inorganic salts such as lithium chloride or sodium nitrate, with melting temperatures above 500 °C, may be more appropriate.

The latent heat of fusion is another crucial thermodynamic property of PCMs. The amount of energy transferred between the PCM and the working fluid or system surfaces is determined by the latent heat. The higher the latent heat, the more energy the PCM can store or release during the phase change process. For instance, paraffin wax has a higher latent heat of fusion compared to other low-cost PCMs, making it an excellent option for thermal energy storage applications.[76,82]

Thermal conductivity is another essential parameter to consider when selecting a PCM. Improving thermal conductivity enhances the energy storage/release rate. This can be achieved by using composite PCMs, adding additives such as nanoparticles to pure PCMs, and/or PCM confinements. For example, adding carbon nanotubes to paraffin wax has been shown to improve its thermal conductivity significantly.

Lastly, thermal stability is an essential parameter to consider when selecting a PCM. The PCM should retain its latent heat and temperature as much as possible after several thermal cycles to ensure a congruent melting process.

2.4. Confinement strategies of PCMs

To improve the thermal conductivity of organic PCMs, researchers have proposed the use of thermally conductive micro-to-nano additives such as carbons, metals, and metal oxides.[71] This approach aims to enhance the thermal properties and performance of PCMs; however, a significant challenge in thermal energy storage management is the potential for liquid phase leakage even when these additives are integrated into PCMs. To this end, one promising solution is PCM confinement, which involves encapsulating PCMs within multiscale ESI. This approach has revolutionized the development of multifunctional and shape-stabilized thermal management systems. Two primary methods of PCM confinement are microencapsulation and nanoencapsulation.[83–85] In microencapsulation, PCMs are confined within a shell made of

organic, inorganic, or polymeric materials. On the other hand, nanoencapsulation involves infiltrating PCMs into porous structures such as aerogels to create form-stable structures. Both methods offer a versatile solution to managing thermal energy storage while maintaining high heat storage performance.[40,86–88]

Depending on the dimensions of the supporting materials, confinement strategies are categorized into four subclasses, including core–shell (0D), longitudinal (1D), interface (2D), and porous (3D) confinements.[89] 0D confinement is defined as encapsulating PCMs with a protective layer through a core–shell structure, while 1D confinement is based on embedding PCMs into the inner cavity of nanofibrous materials such as CNTs. It is also possible to lock PCMs between the layers of various 2D nanomaterials, *e.g.*, graphene, MXene, and h-BN, through the interfacial interaction of the nanoparticles' surface and PCM molecules. Finally, in 3D confinement, aerogels are used as a template or holder to host PCMs in the interconnected nanoporous framework. Among various approaches for confinement, the encapsulation of PCMs within aerogels has emerged as a highly effective method for mitigating the issue of liquid phase leakage, as evidenced by Table 1. Furthermore, the resulting aerogel-based composite PCMs acquire the versatile

Table 1 A summary of the thermophysical properties and noteworthy practices for confined PCM composites

Type of confinement	Supporting material	PCM	K_c[a] (W m^{-1} K^{-1})	T_m[b] (°C)	ΔH_m[c] (J g^{-1})	Key points	Ref.
0D	Silica	Na_2SO_4-10H_2O	—	—	180.7	Subcooling of salt hydrate suppressed	90
	Silica	Octadecane	—	26.5–27.9	93.2–107.5	Confinement causes significant shift in crystallization points	91
	Silica	Stearic acid	—	84.9	276–286	Formation of stable H-bonding increases latent heat by 36.9%.	92
	Al_2O_3	Paraffin wax	0.253	62.6	137	CuO and Al_2O_3 nanoparticles reduce supercooling of PCM by 40% and 31.42%, respectively	29
	CuO	Paraffin wax	0.289	62.2	134		
	AlOOH	Palmitic acid	0.16–0.84	12.7–16.0	19.0–27.8	Melting temperature decreases by more than 50 °C.	93
1D	Cellulose acetate	PEG	—	60.6–69.1	0.5–56.7	The confinement dimension had an influence on the crystallization of PEG.	94
	CNT	Paraffin wax	—	46.9	26.5	A relatively wide working temperature range.	95
	CNT	Paraffin wax		49	123.9	Near the inner wall of the CNTs, paraffin molecules displayed an organized structural arrangement.	96
2D	GO	PEG	—	69.6	—	The freezing point of PEG has been decreased by 14 °C, while the melting temperature remains unchanged.	97
	GO/$Ti_3C_2T_x$	Stearic acid	—	98.7–98.8	108.5–139.3	The confinement raises the activation energy required for crystallization of stearic acid, resulting in the creation of distinct layers such as non-phase transition layer, transitional confinement layer, and proximate bulk layer.	98
3D	Graphene/ polyvinylidene fluoride-hexafluoropropylene (PVDFHFP) aerogel	Paraffin wax	0.28–0.32	28	154.6	The composite material that was developed demonstrated exceptional thermal properties, long-lasting cycle stability, impressive flexibility, and remarkable solar-thermal conversion capability. Moreover, the composite PCM exhibited a phase change enthalpy of 154.64 J g^{-1} and maintained its stability even after undergoing 500 cycles of heating and cooling.	99
	Polyimide/graphene/Fe_3O_4 hybrid aerogel films	PEG	0.12–0.22	~65	158	The hybrid aerogel films showcased a remarkable ability to achieve a high loading capacity of PEG reaching almost 90 weight percent, thanks to their unique macroporous structure and extensive pore volume. The resulting composite PCMs demonstrated exceptional stability even after being subjected to 500 consecutive heating-cooling cycles ranging between 0 and 100 °C. This multifunctional structure offers promising prospects in the fields of EMI shielding and thermal management.	100
	Cellulose nanocrystal/konjac glucomannan/ $Ti_3C_2T_x$ aerogel	Paraffin wax	—	52.9	215.7	The findings indicate that the composite PCMs obtained possess significant reusable stability, excellent EMI shielding properties, and exceptional capabilities for managing thermal energy.	101
	Polyimide/phosphorene (PR) hybrid aerogel	PEG	—	~62–65	150	The prepared composite material possesses a flexible and foldable nature, and exhibits distinctive features that are designed for infrared stealth and thermal camouflage purposes.	56

[a] Thermal conductivity of composite PCM. [b] Melting temperature. [c] Melting latent heat.

properties of aerogels, thereby broadening the potential scope of their applications.[89]

3. Aerogels

Aerogels are a class of synthetic porous ultra-lightweight material derived from a gel. For the fabrication of aerogels, the liquid component of the gel is replaced with gas while maintaining the dried structure without significant collapse of the spatial network.[102,103] Benefiting from exceptionally high porosity, large specific surface area, and ultra-low density, aerogels have been funded for many applications in aerospace engineering, energy harvesting, energy storage, tissue engineering, and environmental remediation applications.[104–107] Subsequently, having entered the realm of nanotechnology by coupling nanomaterials with a variety of matrix materials, multifunctional composite aerogels have advanced in diverse applications ranging from thermal insulation to pollutant detection.[108,109] Amongst all, owing to superb thermal properties, mechanical flexibility, and being atomically thin, the incorporation of 2D-nanomaterials like graphene, MXene, transition metal dichalcogenides (TMDCs)/transition metal oxides (TMOs), carbon nitride (CN), and BN into aerogels has strikingly attracted interest in recent years.[107,110–115] For example, carbon containing nanomaterials such as graphene and MXene have been incorporated into aerogels to augment the electrical conductivity and performance for applications such as supercapacitors, sensors, batteries, field-effect transistors, photodetectors, photovoltaic modules, energy storage devices, catalysis, and EMI shielding, to mention a few.[116–124]

In recent years, aerogels of 2D nanomaterials have emerged as a significant milestone in developing high-performance composite PCMs due to their remarkable physical, textural, thermal, and mechanical properties. Ultra-low density is one of the exceptional features of these aerogels that make them ideal for the fabrication of composite PCMs.[125] To this end, lightweight composite PCMs are highly desirable for energy storage applications, as the energy storage density of composite PCMs, expressed as phase change enthalpy, typically decreases with an increase in the content of supporting materials.[89]

It is worth noting that 2D nanomaterials aerogels with hierarchically porous structures, high porosity, and large specific surface area can accommodate a large quantity of PCMs, resulting in ultra-high PCM loading and increased energy storage capacity.[126,127] In this regard, mesopores are best suited for PCM adsorption and shape stabilization due to their considerable surface tension and capillary forces. On the other hand, micropores restrict the molecular chain movement of PCMs, while macropores lack sufficient capillary forces to retain liquid PCMs. Furthermore, modifying the functional groups on the surface of 2D nanomaterials aerogel hierarchical structures can enhance the compatibility between aerogel surface chemistry and PCMs, resulting in significantly improved shape stability and increased PCM loading.[128,129]

Another important factor in fabricating 2D nanomaterials aerogel-based composite PCMs is their unique mechanical properties. 2D nanomaterials aerogels with and sometimes without reinforcement with various polymers are known for their stable porous interconnected networks that showcase remarkable mechanical performance under external compressive forces. The 3D confinement provided by these flexible skeletons can further expand the functionality of PCMs in advanced thermal management applications, such as thermoregulating textiles, wearable devices, and shape memory materials.[55]

The following sections highlight recent trends regarding 2D nanomaterial-based functional aerogels and their fabrication processes. The guidelines provided in this section will be used in Section 4 to evaluate the most recent fabrication strategies of aerogel-based composite PCMs.

3.1. An overview of aerogel fabrication

3.1.1. Drying approaches

3.1.1.1. Freeze-drying. Drying is one of the most common methods used in the fabrication of free-standing constructs. However, during the normal drying process, capillary forces that arise from the vaporization of solvent molecules can lead to the collapse of pore structures and impact the textural properties of aerogels. To avoid this phenomenon, the freeze-drying method can be used to minimize the stresses on the pores.[130,131] In this method, the solvent, which is typically water for 2D materials, is frozen and then sublimated under the solvent triple point condition, resulting in the evaporation of frozen solvent molecules without any substantial stress or damage to pore structures.[132]

The instrument and aqueous precursor features before drying are the main factors that influence the properties of aerogels prepared by freeze-drying. Instrument considerations include chamber pressure, drying and freezing temperature, freezing rate, and mold type. For instance, it is important to set the freezing temperature between the glass transition temperature and the melting temperature of ice since this parameter affects the density of the aerogels. The freezing rate can also be considered a critical effecting instrument parameter during freeze-drying. Based on the report provided by Yan *et al.*,[133] the carbon nanotubes (CNTs)/chitosan composites prepared at lower freezing rates exhibited better mechanical properties than those at higher freezing rates. This result is ascribed to the formation of thicker lamellas and fewer dendrites at lower freezing rates.

On the other side, the physiochemical properties of precursors also have a significant role in the characteristics of aerogels. For this aim, three main pre-treatment methods, *e.g.*, chemical-induced gelation, freeze-casting, and interfacial assembly, that affect the properties of the precursor before freeze-drying are explained in the following sections.

3.1.1.1.1. Chemical-induced gelation. The development of aerogels' homogeneous networks depends on the uniform distribution of additives and nanoparticles throughout the system. Usually, the chemical-induced gelation process generates stable media with uniform distribution of nanoparticles before the drying process. Gelation occurs when colloidal particles in a sol or solution are joined to create a spatial

framework under specific temperature and pressure conditions, and the spaces of the structure are filled with a proper liquid as a dispersing phase. During the gelation process, when the concentration of nanoparticle suspensions exceeds the critical gel concentration, the attractive and repulsive forces between the sheets become unbalanced.[134,135] As a result, the dispersion phase will become viscous and transform into an elastic colloid capable of withstanding more pressure, which is beneficial for the structure's stability.[136]

An overview of chemical-induced gelation of 2D nanomaterials-based structures is shown in Table 2. Reduction of graphene oxide (GO) using chemical agents is one of the strategies for the self-assembly or gelation of GO nanosheets.[137] To date, many reduction agents, including vitamin C,[138] hydrazine,[139] sodium borohydride,[140] ascorbic acid,[141] potassium hydroxide,[142] and pyrogallol,[143] have been widely used for the reduction and gelation of GO suspensions. Furthermore, combining chemical reduction and hydrothermal processes can accelerate the removal of oxygen-containing functional groups and the chemical-induced assembly of reduced graphene oxide (rGO) nanosheets. In 2019, Shen *et al.*[144] developed graphene aerogels using a hydrothermal-assisted method. For this aim, a proper

Table 2 Beyond chemical induced gelation for fabrication of 2D based nanomaterial aerogels

Material	Gelation agent	Preparation technique	Other	Ref.
rGO	EDA	Chemical-induced gelation Freeze-drying	EDA was used as a reducing agent and crosslinker.	175
rGO	EDA	Chemical-induced gelation and cross-linking Solvent exchange Freeze-drying	EDA was used as a reducing agent and crosslinker. The prepared GO aerogel beads were thermally reduced.	176
$Ti_3C_2T_x$	EDA	Chemical-induced gelation Freeze-drying	EDA was used as a crosslinker to assemble MXene nanosheets.	177
rGO/Pd	Ethylene diamine tetra acetic acid (EDTA)	Chemical-induced gelation Freeze-drying	GO aerogels were first reduced by hydrazine vapor and then thermally annealed under hydrogen gas.	178
N-doped rGO	EDA Diethylenetriamine (DETA) Tetraethylenepentamine (TEPA)	Chemical-induced gelation Freeze-drying	The bonding state of nitrogen atoms is related to the type of reducing agents.	179
$Ti_3C_2T_x$/GO	GO	Chemical-induced gelation Electrostatic spinning Freeze-drying	GO was used as a crosslinker for $Ti_3C_2T_x$.	180
$Ti_3C_2T_x$/rGO	GO	Chemical-induced gelation Freeze-drying Chemical reduction	GO was used as a crosslinker for $Ti_3C_2T_x$. The fabricated aerogels were chemically reduced *via* a mixture of hydroiodic and acetic acids.	181
GO/PVA	PVA	Chemical-induced gelation and cross-linking Freeze-drying	PVA was used as a cross-linking agent.	182
rGO	Octadecylamine (ODA)	The GO solution was dripped into a coagulation bath to achieve ODA and ethanol to achieve rGO hydrogel beads. Freeze-drying	ODA was used as a reducing agent and crosslinker. The prepared GO aerogel beads were thermally reduced.	183
$Ti_3C_2T_x$/calcium alginate	Ca^{2+}	Chemical-induced gelation Vacuum-assisted-filtration Freeze-drying	Divalent Ca^{2+} ions were used as a crosslinker for $Ti_3C_2T_x$	184
$Ti_3C_2T_x$/GO/ sodium alginate	GO/Ca^{2+}	Chemical-induced gelation Freeze casting Freeze-drying	Divalent Ca^{2+} ions were used as the main crosslinker for $Ti_3C_2T_x$. GO was also effective for cross-linking $Ti_3C_2T_x$ sheets.	185
$Ti_3C_2T_x$	Fe^{2+}	Chemical-induced gelation Freeze-drying	Divalent Fe^{2+} ions were used as a cross-linker for $Ti_3C_2T_x$	186
Mg^{2+}–$Ti_3C_2T_x$	Mg^{2+}	Chemical-induced gelation Freeze-drying	—	187
Fe^{3+}–$Ti_3C_2T_x$	Metal ions	Chemical-induced gelation Freeze-drying	Different metal ions, *e.g.*, Fe^{2+}, Al^{3+}, Co^{2+}, Ni^{2+}, Mg^{2+}, Ca^{2+}, Mn^{2+}, Zn^{2+}, were used as chemical crosslinkers for MXene assembly.	156
rGO/MoO_2	L-Ascorbic acid	Chemical-induced gelation Freeze-drying	L-Ascorbic acid was used as a reducing agent and cross-linker.	143
rGO/Au	L-Ascorbic acid/$Na_2B_4O_7$	Chemical-induced gelation Freeze-drying	$Na_2B_4O_7$ was used as an enhancer for reducing GO.	144
rGO	Vitamin C	Chemical-induced gelation Freeze-drying	Vitamin C was used as a reduction agent. After freeze-drying, the samples were thermally annealed.	142
rGO	$NaHSO_3$	Chemical-induced gelation Freeze-drying	$NaHSO_3$ was used as a reducing agent and crosslinker. The prepared GO aerogel beads were thermally reduced.	188
$Ti_3C_2T_x$/polyimide	—	Chemical-induced gelation BDFC Freeze-drying	First, the polyamic acid was synthesized and mixed with $Ti_3C_2T_x$ to fabricate aerogels. The prepared structures were then thermally annealed to complete the imidization process, *i.e.*, the formation of polyimide.	189

content of L-ascorbic acid was added to the GO suspension as a reduction agent, and then the resulting suspension underwent hydrothermal reduction at 180 °C for 14 h. Eventually, the aerogel composites were fabricated by freeze-drying (−50 °C) the frozen rGO hydrogels.

Apart from reducing agents, cross-linking materials can facilitate GO gelation by increasing binding forces within GO sheets. Hydroxyl-containing, *e.g.*, poly(vinyl alcohol) (PVA),[145] oxygen-containing, *e.g.*, hydroxypropyl cellulose[146] and polyethylene oxide,[147] and nitrogen-containing, *e.g.*, polyamines,[148] materials can be considered organic cross-linkers for efficient gelation of GO. From the molecular-scale point of view, the aforementioned polymeric materials can generate hydrogen bonds around GO sheets, which causes an enhancement in the viscosity of the GO suspension. Interestingly, a novel rGO aerogel was synthesized *via* a double-crosslinked technique.[149] In this report, both ethylenediamine (EDA) and lysine were added to the GO dispersion, and then the hydrogels were achieved under thermal treatment. Subsequently, the frozen hydrogels were freeze-dried at −40 °C to achieve free-standing aerogels. Furthermore, the obtained results indicated that the double-crosslinked technique is capable of improving the compression property of aerogels compared to the single cross-linking method, *i.e.*, only EDA addition.

On the other hand, hydrothermal gelation without cross-linkers is hard to achieve for MXene nanosheets due to their superhydrophilic nature.[150] As a result, another mediator, *i.e.*, cross-linker, in the hydrogel matrix is frequently required to counteract the hydrophilic nature of MXenes and sustain the 3D assembly of the 2D nanosheets.[151] For example, some studies introduced GO as a gelation agent for MXenes. In detail, GO manipulates interfacial contacts with MXene sheets instead of point-to-plane interactions, leading to a reduction in electrostatic repulsion between MXene nanosheets and GO and thus allowing self-assembly of MXene sheets in the anisotropically-assembled GO structure. GO cross-linking assembly was used to prepare S, N co-doped rGO/MXene aerogels under hydrothermal conditions.[152] Due to the reductive feature of MXene induced by surface termination groups, rGO nanosheets were produced by adding GO to the MXene solution. To further improve the quality of aerogels produced through the GO-assisted cross-linking approach, Chen *et al.*[153] used ethanediamine as a secondary reducing and cross-linking agent. In this strategy, ethanediamine, *i.e.*, an amine-rich agent, opens the epoxy rings on GO nanosheets to facilitate the formation of oxygen-dangling bonds. Subsequently, MXenes are linked to these dangling bonds, resulting in robust 3D rGO/MXene assemblies.[154]

The utilization of GO as an agent in the MXene gelation process has proved to oxidize MXenes, causing partial degradation of hydrogels and lowering their qualities.[155] Therefore, to limit the oxidation effects, a quicker gelation procedure is required to accelerate the separation of MXene from water and efficiently decrease the degree of nanosheet restacking. The use of metal ions as cross-linkers has demonstrated excellent potential in the fast gelation of MXene suspension. Zhou *et al.*[156] developed quick MXene hydrogels using different metal ions, *e.g.*, Co^{2+}, Ni^{2+}, Fe^{2+}, Al^{3+}, Mg^{2+}, Ca^{2+}, Mn^{2+}, and Zn^{2+}, as cross-linkers to fabricate 3D MXene-based aerogels. The metal ions acted as 'chemical glues' and formed strong bonds with hydroxyl functional groups on the surface of MXene. Accordingly, the generated interlinks are able to reduce the hydrophilicity of MXene sheets and accelerate the gelation rate of MXene. Therefore, MXene sheets are preserved from oxidation due to the short gelation process, *i.e.*, a few minutes, after metal salts addition to MXene suspension. It is worth noting that monovalent metal ions such as K^+ have lower hydration energy than that of covalent and trivalent ions, leading to the coagulation of MXene sheets and a failing gelation process.[157]

3.1.1.1.2. Freeze-casting. The freeze-casting method was introduced for the first time by Fukasawa *et al.*[158] In this approach, they attempted to prove the influence of the formation and growth of ice crystals on the porous ceramic's mechanical properties. The freeze-casting method employs the ice crystals as a template during the water solidification, leading to effective phase separation. This method is followed by subsequent extraction of the frozen solvent by sublimation, leading to the generation of a 3D hierarchical network with aligned porosities.[159] Freeze-casting is also used for engineering the architecture of 2D nanomaterial aerogels, where nanosheets are stacked between ice crystals and form continuous 3D networks after sublimation.

In traditional freeze-casting, also known as the unidirectional casting, heat is conducted in the axial direction while the radial direction is non-conductive. This allows ice crystals to form along the established temperature gradient, such as vertically from the bottom of the template as it cools down.[160] In this regard, Wicklein *et al.*[161] fabricated micro-honeycomb GO-based aerogels through unidirectional freeze-casting of GO suspensions. The GO suspension was poured into a mold and placed on top of a copper rod that was in contact with liquid nitrogen. Finally, the suspensions were solidified at different cooling rates ranging from 1 K min^{-1} to 15 K min^{-1} and then freeze-dried to obtain robust aerogels.

Bidirectional freeze-casting (BDFC) is one of the casting approaches suitable for fabricating large-sized, *i.e.*, centimeter-scale, 3D networks of nanomaterials with a high degree of control on the ordering of pore structures. In other words, this technique allows the ice to form in both vertical and horizontal directions by controlling nucleation and growth of ice crystallization under dual temperature gradients.[162] Wang *et al.*[163] fabricated centimeter-scale radiating GO aerogels using BDFC with two perpendicular temperature gradients, *i.e.*, bottom to top and outside to inside. After the freeze-casting process, aerogels were achieved through freeze drying at −108 °C and 0.001 MPa for 48 h.

3.1.1.1.3. Interfacial assembly. The assembly of nanomaterials at the interface of two immiscible liquids is an emerging platform for the fabrication of soft-functional materials, where the inherent characteristics of nanoparticles can be locked into the final constructs. In this technique, decreasing the Helmholtz free energy drives solid particles toward the liquid–liquid interface.[164] However, the energy of the liquid interface in the case of nanomaterials is much lower than micrometer-sized colloidal particles. Hence, nanoparticle assemblies at liquid–liquid interfaces tend to be unstable due to their dynamic

nature, dependence on size, and association with the constant adsorption and desorption of nanomaterials.[165] To overcome these instabilities, the addition of oligomeric/polymeric ligands at the oil–water interface has been recognized as an efficient way to increase nanoparticle interfacial performance. In this strategy, the nanoparticles and ligands interact at the interface and create nanoparticle surfactants, allowing the nanoparticles to jam at the interface.[166]

Interfacial assembly and jamming of nanoparticles at the liquid–liquid interface result in non-equilibrium forms of one liquid phase in another immiscible liquid. Note that these generated structured liquids are programmable due to the ability to be un-jammed and re-shaped.[167–169] Such a programmable fabrication platform can be used as an innovative pre-treatment for large-scale fabrication of robust aerogels with well-defined micro- to macro-scale characteristics. Kamkar *et al.*[170] fabricated ultra-flyweight graphene-based aerogels with a density of $\sim$0.15–1.2 mg cm^{-3} using structured liquids of GO as a template. For this aim, aqueous suspensions of GO were injected into a non-polar domain containing PSS-[3-(2-aminoethyl)amino]propyl-heptaisobutyl substituted POSS (POSS-NH_2) and hexane to form worm-like structured liquids. In this case, the co-assembly of GO and POSS at the liquid–liquid interface generates an interfacial skin that stabilizes the aqueous phase in a non-equilibrium shape. The fabricated structures were finally kept in a freezer for 24 h and then freeze-dried for two days to construct ultra-flyweight aerogels of GO.

3.1.1.2. Supercritical drying. Supercritical drying is another method for creating aerogels at temperatures and pressures above the critical point of solvents. As the conditions exceed the critical point, the liquid phase turns into a supercritical fluid, eliminating the difference between liquid and gas phases and greatly reducing the surface tension in the solid pores.[171] Accordingly, the pores were well-preserved during drying due to the elimination of the surface tension and capillary forces. The supercritical drying process is proven to be very effective in fabricating highly porous structures with ultra-low shrinkage or cracking during drying by operating beyond the liquid–gas boundary state.[172] For instance, Cheng *et al.*[173] developed mechanically robust rGO aerogels with a relatively large specific surface area through supercritical drying. After preparing 3D rGO-based hydrogels through hydrothermal treatment and chemical reduction, the obtained gels were dried with supercritical ethanol for almost one week at operating temperature and pressure of 250 °C and 8 MPa, respectively.

3.1.1.3. Ambient temperature drying. As explained in the previous sections, supercritical-drying and freeze-drying approaches require specific equipment to achieve vacuum pressure in a few centimeter cells. Hence, their applications are limited to the fabrication of centimeter-scale aerogels, and their operating costs are high. Accordingly, ambient temperature drying, also known as air-drying, can be employed to fabricate cost-effective and large-scale aerogels of 2D nanomaterials. However, the shrinkage of liquids during evaporation and preservation of pores after drying remains challenging; therefore, suitable pre-treatment techniques should be applied to minimize the capillary forces within the pores. Recently, Yang *et al.*[174] fabricated large-scale structure-intact graphene aerogels with an approximate size of 1 m^2 and a density of 2.8 mg cm^{-3} through ambient temperature drying. This method introduced the microbubble template to confine the GO sheets within microbubble gaps and attain structure-intact graphene hydrogel. Then, the fabricated hydrogels were frozen for 4–6 h at −18 °C and dried at 60 °C in the air for almost 12 h. The resulting aerogels showcased exceptional elasticity and ultra-low density of $<$10 mg cm^{-3}, comparable to the best practices reported for freeze-dried or critically dried graphene samples.

3.2. 2D nanomaterials in aerogel fabrication

2D nanomaterials are single or multilayered sheet-like structures with strong in-plane bonds and weak van der Waals forces between sheets.[190,191] Graphene, metal oxides and hydroxides, dichalcogenides, polymers, BN, phosphorene, and MXenes are prime examples of 2D nanomaterials that have been synthesized through extraction, exfoliation, chemical or physical vapor deposition, and numerous wet chemical strategies.[191,192] Benefiting from their distinct physical and chemical properties and straightforward surface functionalization, 2D nanomaterials have been vastly utilized to fabricate network-like aerogels with hierarchically arranged frameworks.[193,194]

3.2.1. Graphene-based aerogels. Graphene is a superstar of carbonaceous nano allotropes consisting of either one or a few layers of atoms tightly packed in a hexagonal 2D honeycomb lattice. It is highlighted as the strongest material known today, with intrinsic tensile strength and Young's modulus of 130 GPa and 1 TPa, respectively.[195] 2D graphene nanosheets also exhibit unique thermal conductivity (5300 W m^{-1} k^{-1}), optical transmittance ($\sim$97.7%), exceptionally large specific surface area ($\sim$2600 m^2 g^{-1}), inherent hydrophobicity, and high carrier mobility, opening numerous opportunities ranging from smart electronics to thermal management systems.[196–198] However, challenges regarding the synthesis of pristine graphene, along with their tendency to re-agglomerate into graphite-like powders due to the strong π–π stacking and van der Waals interactions between them, dramatically limit its application in aerogel fabrication.[195,199,200] These problems have given rise to the use of GO-based aerogels.[201,202]

GO is readily dispersible in many solvents, its physicochemical properties can be fine-tuned over a wide range, and it can be easily assembled into 3D gel networks upon further chemical/electrochemical treatments.[202] However, GO is electrically insulative and, compared to pristine graphene, suffers from high oxidation levels and lattice defects. Therefore, GO or its 3D scaffolds, *e.g.*, gels and aerogels, usually undergoes chemical, thermal, or electrochemical reductions to approach charge mobility and graphene-like characteristics.[195,201,203] For instance, Hu *et al.*[202] have employed chemical-induced gelation to produce ultra-light, yet highly compressible aerogels, by a two-step process. In brief, monolithic functionalized graphene hydrogels were produced by adding EDA aqueous solution as a weak reduction agent to the GO suspension. The obtained structured hydrogels were then converted into

GO-based aerogels through lyophilization. Finally, as a secondary reduction step, microwave irradiation was used to reduce the amount of oxygen-containing functional groups, resulting in ultra-lightweight graphene-based aerogels. After microwave irradiation treatment, the black-colored aerogels turned into metallic gray, while the 3D network was well preserved due to the strong bonding between the building blocks. The scanning electron microscope (SEM) images of the prepared graphene-based aerogels showcased an interconnected foam-like structure with pores ranging from tens to hundreds of micrometers. The cell walls were composed of assembled graphene sheets that were formed during the freezing step, where the individual sheets were densified by the formation of ice crystals. It is worth noting that 1D wrinkles or crumbled regions across the surfaces of assembled graphene sheets promote the elasticity of aerogels that were retrieved even after 90% compression without fracture.

Another versatile technique for developing highly compressible and mechanically robust graphene-based aerogels is freeze-casting. The typical freeze-casting technique of GO involves unidirectional freezing of aqueous suspensions in a mold placed on the top of a cold substrate, which results in a lamellar-structured graphene aerogel.[204–206] However, when simultaneous freezing happens at the sides and bottom of the mold, a radiated GO aerogel with cross-linked channels whose width increases with distance from the center can be achieved (Fig. 1a–c).[207–209] This approach, also known as BDFC, has been employed by Wang *et al.*[163] to generate radially aligned and centrosymmetric structured GO aerogels with enhanced elasticity and oil absorption characteristics. After chemical reduction with hydrazine vapor, exceptional compressibility with only 8% permanent deformation after 1000 cycles under the compressive strain of 50%, the unique oil absorption capacity of 86.6 to 374.7 g g^{-1}, and excellent fire retardance without any structural collapse were observed for these aerogels. Aside from pure GO aerogels, this method has also been employed for fabricating various nanocomposite aerogels such as GO/CNFs with radially ordered texture and GO/chitosan with either radial or spiral pattern, introducing BDFC as a universal platform for composites and beyond (Fig. 1d).

In another study, BDFC was also used to assemble PVA and GO sheets into biomimetic aerogels resembling the Thalia dealbata stem-like structure (Fig. 1e–g). These aerogels not only mimic the architectural features of the plant stem but also showcase exceptional flexibility and mechanical stability. In brief, a polydimethylsiloxane (PDMS) wedge with a slope angle of around 15° between the cooling stage and precursor suspension was used to generate dual temperature gradients *i.e.*, both horizontal (ΔT_H) and vertical (ΔT_V), for BDFC. Ice crystals nucleated at the bottom of the PDMS wedge and then grew under perpendicular temperature gradients to create a hierarchical 3D structure (Fig. 1h–i). Upon thermal reduction under 800 °C, an exceptional electrical conductivity of 2–14 S m^{-1} and unusual strength/resilience were achieved for these constructs. The resilience of this construct involves retaining nearly 85% of its original compressive strength after 1000 cycles and supporting more than 6000 times its own weight with ~50% strain.[210]

Despite the abovementioned advances in the fabrication of highly compressible graphene-based aerogels, these studies suffer from numerous limitations in scalability and controlling structures from micro to macro scale.[211–215] As a paradigm shift, emulsion-sculpting and foaming/microbubble templating have been recently introduced to address these challenges.[216,217] For example, a surfactant-foaming sol–gel method was used to achieve macroscopically ordered and scalable graphene aerogels (~1 m^2). This method introduced the microbubble template to confine the GO sheets within microbubble gaps to attain structure-intact graphene hydrogel. The homogeneous microbubbles were developed by rapidly stirring alkyl polyglucoside/GO aqueous dispersion. The foamed GO suspension was reduced by ascorbic acid, simply frozen, air-dried, and annealed at 200 °C to fabricate a smooth and intact aerogel without any evident shrinkage (Fig. 2a–d). The obtained graphene-based aerogel demonstrated an ultra-low density of 2.8 mg cm^{-3}, a compressive strain of up to 99%, and a high thermal decomposition temperature of T_{max} = 735 °C in the air (Fig. 2f). Moreover, these aerogels were introduced as compressive force absorbers (force => 700 N) and as unique absorbers of oils or hazardous solvents, *e.g.*, capacity = 260–570 g g^{-1}.[174] In another remarkable study, Kamkar *et al.*[123] fabricated structured liquids of GO in hexane/PSS-[3-(2-aminoethyl)amino]propyl-hepta-isobutyl substituted POSS (POSS-NH_2) and used them as a template for producing an advanced type of ultra-flyweight aerogels. In this approach, worm-like structured liquids were obtained by streaming GO suspension into hexane/POSS (Fig. 2f–h). Furthermore, the stability of GO liquid jets was explained through interfacial co-assembly of GO/POSS, leading to a mechanically robust and elastic interfacial skin with a high binding energy that can withstand compressive force. Upon freeze-drying and dual chemical/thermal reduction of these interfacially driven constructs, a novel class of graphene-based aerogels with exceptionally low density in the range of ~0.25 to ~4 mg cm^{-3}, high electrical conductivity, and multiscale porosities (micro- and macro-scaled) were achieved (Fig. 2i–k). These structures were also used as highly compressible and high-performance EMI shields with a specific shielding effectiveness of ~24 000 dB cm^2 g^{-1} (shielding 99.8% of the incident wave).

3.2.2. MXene-based aerogels. MXenes are a class of 2D metal carbides and nitrides with two or more layers of transition metal (M) atoms in their structure. The general formula of MXene is $M_{n+1}X_nT_x$, where M represents the transition metal site, X denotes carbon or nitrogen sites, and T_x (where x is variable) represents surface terminations of the outer transition metal layers. Depending on the number of transition metal layers, the n value in the formula varies from 1 to 4.[218–223] These newly discovered 2D materials are mainly produced through the top-down synthesis approach by etching the A-layer atoms (*e.g.*, Al, Si, Ga) of MAX phases, *i.e.*, a group of layered, hexagonal-structure ternary carbides and nitrides with the general formula of $M_{n+1}AX_n$.[224] Up to now, several types of MXenes have been successfully synthesized, and dozens more were predicted to exist and studied *in silico*.[150] Amongst all, $Ti_3C_2T_x$ is the easiest to assemble and be used to fabricate multifunctional aerogels.[225,226]

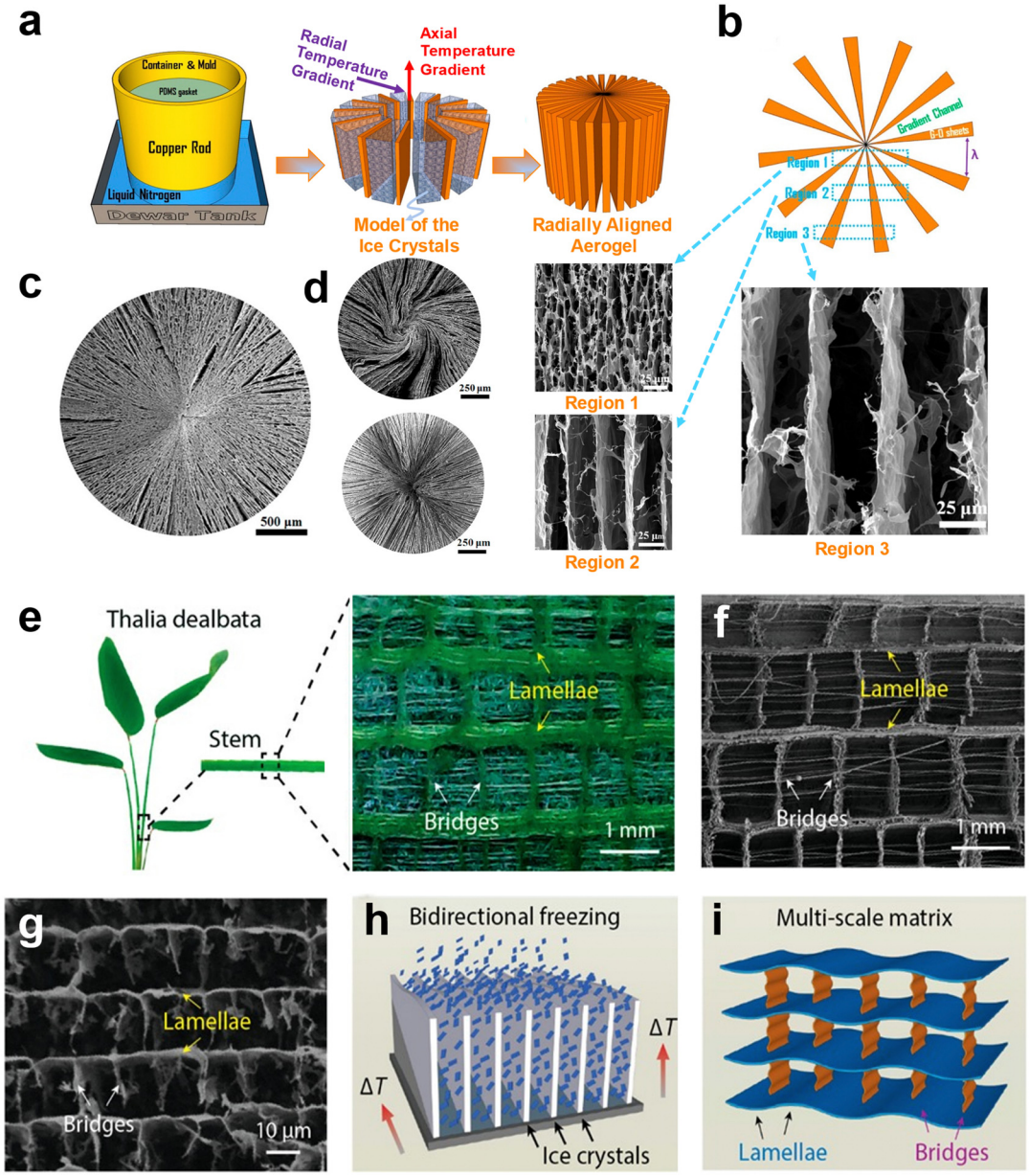

Fig. 1 (a) Schematic illustration of the BDFC method used for developing radially aligned graphene-based aerogels. (b) Cross-section SEM images of the GO-based aerogel. The widths (λ) of channels increase from center to edge, representing a radially aligned structure. (c) SEM image of radially aligned GO aerogel. (d) SEM images of GO/chitosan aerogels with either spiral or radial patterns. (a–d) Reproduced with permission.[163] Copyright 2018, American Chemical Society. (e–g) Optical image of the architecture of the Thalia dealbata stem and corresponding biomimetic GO-based aerogel. (e and f) An oriented lamellar layer parallel to the growth direction with interconnected bridges was observed in the optical and SEM images of the Thalia dealbata stem. (g) The SEM image of biomimetic graphene-based aerogels showcased oriented layers and interconnected bridges similar to those of the Thalia dealbata stem. (h) The formation of the ice crystals in the BDFC *via* a PDMS wedge. (i) The schematic of the as-prepared graphene aerogel in the format of the plant stem. (e–i) Reproduced according to the terms of ACS author choice license.[210] Copyright 2017, American Chemical Society.

Distinct electrical conductivity, hydrophilic nature, and the ability to intercalate cations and store charge led to significant interest in exploring $Ti_3C_2T_x$ for EMI shielding, strain sensing, and energy storage applications.[227,228]

Similar to graphene, MXene-based aerogels also go through various processing steps to achieve better mechanical characteristics. To date, the freeze-casting technique, along with subsequent freeze-drying, is among the most popular fabrication methods of $Ti_3C_2T_x$ aerogels. However, due to the weak van der Waals forces between $Ti_3C_2T_x$ sheets, polymeric binders, *e.g.*, gelatin, cellulose, PVA, *etc.*, are routinely added as a chemical glue to assemble 2D nanosheets and enhance the mechanical characteristics of the final constructs. For instance, in a recent study, gelatin molecules were introduced as a chemical binder to strengthen the interaction between $Ti_3C_2T_x$ nanosheets and fabricate 3D composite aerogels of MXene with

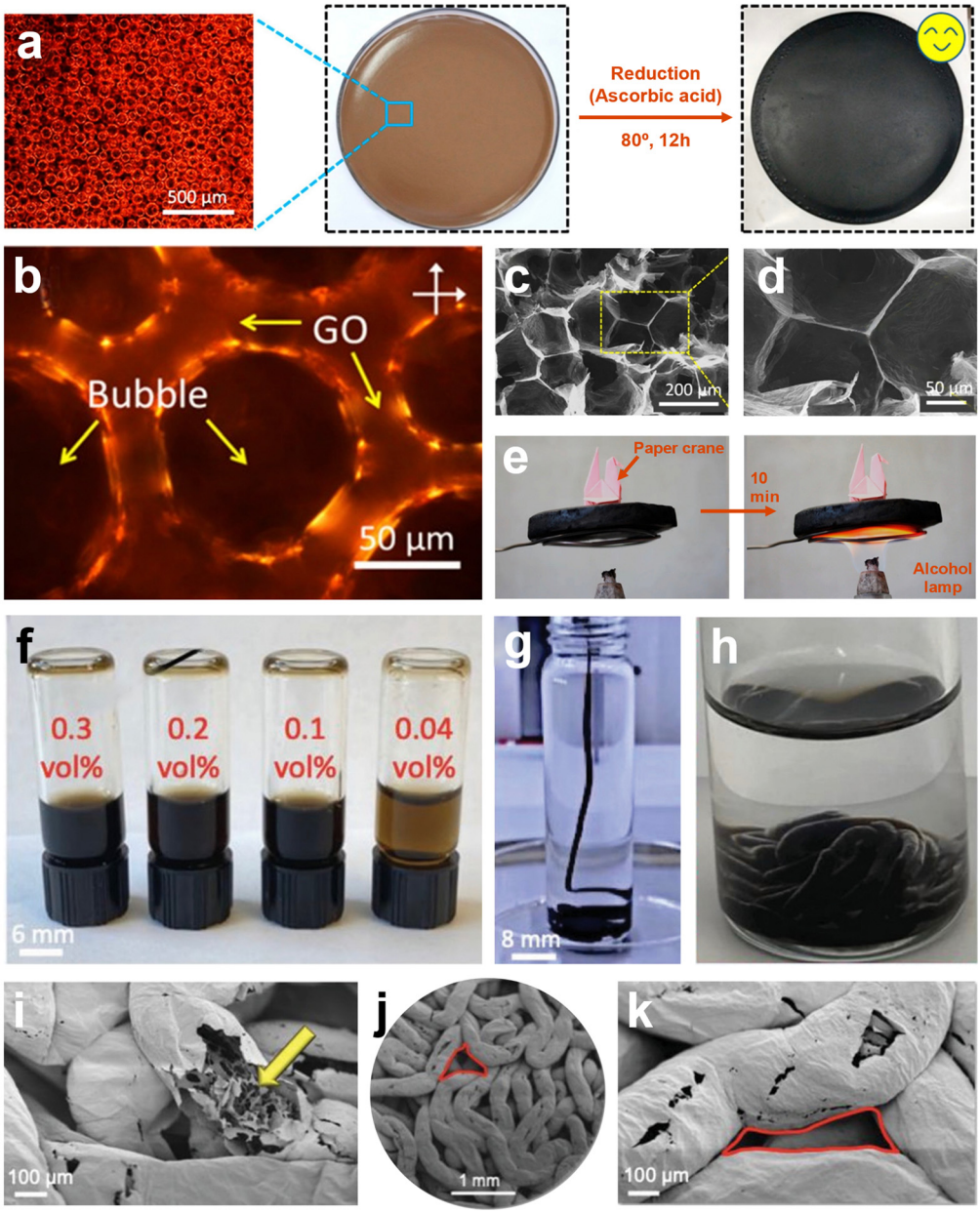

Fig. 2 (a) The surfactant-foaming sol–gel method uses microbubble templates to fabricate uniform rGO aerogels without freeze-drying. (b) Polarized-light optical microscope (POM) image of the foam GO solution showcasing the microbubble template. (c and d) The SEM images of graphene aerogels demonstrate the confined rGO sheets within the template's gaps. (e) Superior thermal stability of rGO aerogels. (a–e) Reproduced with permission.[174] Copyright 2018, American Chemical Society. (f) The GO aqueous inks were used for liquid streaming in the hexane/POSS domain. (g) Streaming GO aqueous suspensions in hexane/POSS. (h) Digital images of GO worm-like structured liquids. The prepared structures showcased dual porosities from (i) micro- to (j and k) macro-scales. (f–k) Reproduced according to the terms of the CC-BY license.[123] Copyright 2022, Wiley-VCH.

much enhanced yet anisotropic mechanical characteristics. In this approach, $Ti_3C_2T_x$/gelatin homogenous suspension was cast into a rectangular aluminum-based Teflon mold and immersed in liquid nitrogen. Ice crystals grew vertically afterward, compelling $Ti_3C_2T_x$ nanosheets and gelatin molecules to be assembled in a parallel direction. Unidirectional freeze-casting followed by a freeze-drying approach endowed lightweight and highly porous $Ti_3C_2T_x$/gelatin aerogel, indicating a −59.5 dB minimum reflection loss at 14.04 GHz with a 6.24 GHz effective absorption bandwidth.[229]

Scaling the unique characteristics of $Ti_3C_2T_x$ nanosheets to functional aerogels without compromising electrical conductivity and/or electrochemical activities is still challenging, particularly because traditional assembly approaches of $Ti_3C_2T_x$ aerogels mainly rely on external binders, which tremendously reduce the functionality of the final constructs. In order to address this challenge, Ding *et al.*[230] developed metal ion-intercalated $Ti_3C_2T_x$ aerogels without polymeric binders showcasing distinctive electrical conductivity of 758.4 S m^{-1}, a large surface area of 140.5 m^2 g^{-1}, and high stability in aqueous

media. In brief, $Ti_3C_2T_x$ suspension was blade coated onto the polystyrene substrate and heated up to 130 °C to form a crumpled-texture $Ti_3C_2T_x$ layer. The fabricated platform was then thoroughly loaded with Mg^{2+} to induce the gelation of $Ti_3C_2T_x$. Mg^{2+}/MXene hydrogels were finally freeze-dried to fabricate biomimetic aerogels featuring the hierarchical texture of Phrynosoma cornutum, the Texas-honored lizard (Fig. 3a–f). The Mg^{2+}/MXene aerogel demonstrated outstanding EMI shielding characteristics, excellent salt adsorption properties in brackish water desalination, and exceptionally high aerial capacitance in quasi-solid-state micro-supercapacitors. In another study, unidirectional freeze-casting was used to assemble PVA and $Ti_3C_2T_x$ nanosheets into biomimetic aerogels resembling the morphology of down feathers in penguins (Fig. 3g–k). After successive oxidation and calcination of pristine $Ti_3C_2T_x$ nanosheets, spectrally modified $Ti_3C_2T_x$ were synthesized. Then PVA and $Ti_3C_2T_x$ were blended and freeze-thawed three times to obtain a hydrogel. After subsequent freeze-casting and freeze-drying, an anisotropic hierarchical structure of horizontally aligned struts with parallel porous alignments was assembled at an angle of $\sim 60^\circ$. Unlike the traditional unidirectional freeze-casting technique, this approach used PVA as an ice-structuring binder to induce dendritic growths of ice crystals from the main trunks. The high viscosity of PVA/calcinated $Ti_3C_2T_x$ suspension and the repeated freezing-thawing process hamper the growth of ice crystals along the temperature gradient and facilitate the formation of transverse ligaments at an angle to the main trunks. Such feather-like micro-porous structures were used for highly efficient solar-powered water evaporators due to their low thermal conductivity of 0.162 W m^{-1} K^{-1} and full-spectrum sunlight absorption of 98.5%.[231]

Interfacial co-assembly and Jamming of $Ti_3C_2T_x$ and POSS-NH_2 at the toluene/water interface is another interesting procedure employed for the fabrication of functional MXene-based aerogels.[235] In this emulation system, $Ti_3C_2T_x$ nanosheets and POSS-NH_2 form an overlapping layer of MXene nanosheets, which offer a robust assembly with excellent mechanical properties upon jamming (Fig. 4a and b). The degree of $Ti_3C_2T_x$ overlap was programmed by increasing the concentration of POSS-NH_2, leading to the tunability of the final constructs. These programmable structured liquids were then used as a template to fabricate lightweight, hydrophobic, isotropic MXene aerogels with unique mechanical and electrical characteristics. Despite the hydrophilic nature of $Ti_3C_2T_x$, these aerogels showcased unique hydrophobicity that stems from the presence of POSS-NH_2 in the liquid template. This hydrophobicity, along with the highly porous structures of the fabricated aerogels, made them promising oil absorbers (Fig. 4c and d). For example, a toluene absorption of up to 9000% is found for these constructs. Furthermore, similar to other $Ti_3C_2T_x$-based aerogels, these interfacially driven morphologies of MXene also demonstrated unique EMI shielding effectiveness of 34.5 dB at the thickness of only 2 mm.[235]

The metal ionic crosslinking technique is another high-paced approach that can be utilized to generate well-patterned $Ti_3C_2T_x$ hydrogels as a template for developing functional aerogels. Through a three-step electro-gelation process, MXene hydrogels were formulated with spatial patterning and controllable resolutions down to 130 μm. First, a series of patterns that defined the final shape of hydrogels were printed on a circuit board. Then, copper, as a sacrificial metal, was electrodeposited on the Au pads of circuit boards. Finally, $Ti_3C_2T_x$ suspension was applied in the cell to accomplish the electro-gelation process, which yielded pre-defined 3D assemblies of MXene. By electrolyzing the copper, Cu^{2+} releases and initiate the electro-gelation process during which electrostatic interactions occur between cations and the $Ti_3C_2T_x$ sheets (Fig. 4e and f). This approach generates complex architecture that cannot achieve through any of the methods described before (Fig. 4g). After freeze-drying, the resultant aerogel featured a lightweight structure with a specific surface area of 68.8 m^2 g^{-1}.[236]

3.2.3. Other 2D nanomaterials for functional aerogels. Although graphene and MXene present remarkable physiochemical properties, other 2D materials have also been used as building blocks of aerogels. Up to now, several 2D nanomaterials, such as h-BN, molybdenum disulfide (MoS_2), and tungsten diselenide (WSe_2), have been synthesized and employed for multifunctional aerogel fabrication.[237] For instance, MoS_2 has been extensively studied as a highly stable and cost-effective nanomaterial that possesses a tunable band gap.[238–240] MoS_2 is usually hybridized with other 2D nanomaterials, including GO, to prepare functional aerogels since MoS_2 nanoflakes alone are unable to form structured scaffolds with a highly effective surface area. These MoS_2/GO aerogels demonstrated unique capability for gas sensing, thermal insulation, and energy storage.[241–243] The potential of MoS_2/GO hybrids was highlighted by Tang *et al.*,[244] where hybrid supercapacitors with complex geometries were fabricated by 3D printing of MoS_2/GO inks. The viscoelastic characteristics and general printability of these hybrid inks mainly relied on GO, while the addition of MoS_2 was introduced as a way to improve the printing resolution and areal capacitance of fabricated structures. Aside from MoS_2/GO inks, 2D GO nanosheets were also employed as a domain for printing other nanomaterials, including 0D silver nanodots and 1D multi-walled carbon nanotubes (MWCNTs). The process of ink fabrication and 3D printing for these hybrid aerogels is shown in Fig. 5a–c. In a typical procedure, negatively charged nanoparticles, *e.g.*, silver, MoS_2, and MWCNTs, were added to the solution of urea, gluconic-δ-lactone, and GO. Upon increasing the temperature, mild hydrolysis of urea happened during solvent evaporation, resulting in the gelation of the hybrid inks. It is worth noting that the secondary nanoparticles were closely bound with micropores of the cross-linked GO sheets upon gelation (Fig. 5d). The prepared inks were then used for 3D printing complex and nonplanar geometries that transformed into functional aerogels upon freeze-drying, chemical reduction, and additional thermal annealing.

Aerogels of 2D h-BN are known for their unique mechanical and thermal characteristics and therefore provide potential avenues for numerous applications, including thermal management systems, gas absorption, infrared insulations, field-effect transistors, photodetectors, photovoltaic modules, energy storage devices,

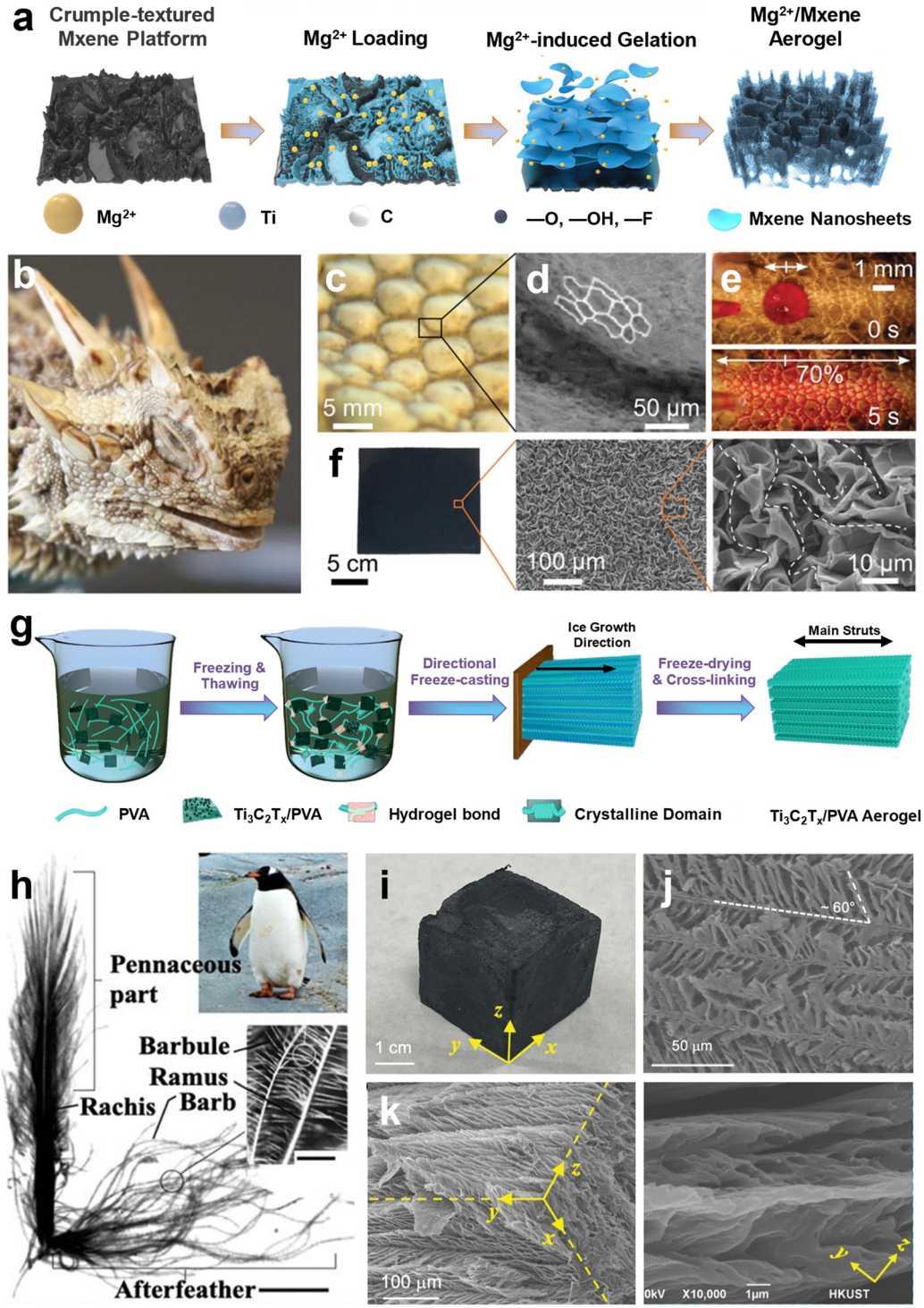

Fig. 3 (a) Schematic illustration of the scalable fabrication of crumpled-texture Mg^{2+}/MXene platform *via* Mg^{2+}-induced gelation method. The fabricated structure resembles the texture of Phrynosoma cornutum's skin. (b) Digital photo of Phrynosoma cornutum. (c and d) Optical and SEM images of micro-ornamentations of lizard's skin that can transport water. Reproduced according to the terms of the CC-BY license.[232] Copyright 2011, Beilstein-Institute. (e) Movement of water in microchannels of Phrynosoma cornutum's skin. (b and e) Reproduced according to the terms of the CC-BY license.[233] Copyright 2015, The Royal Society. (f) Optical and SEM images of crumpled-texture MXene coating after thermal shrinkage. (a and f) Reproduced with permission.[230] Copyright 2021, Wiley-VCH. (g) Schematic illustration of the multifunctional fabrication of feather-like $Ti_3C_2T_x$/PVA aerogels. (h) Digital image of a penguin down-feather depicting structural details in multiscale. Reproduced with permission.[234] Copyright 1999, Academic Press. (i–k) Digital and SEM images of the feather-like biomimetic aerogels of $Ti_3C_2T_x$/PVA. (g and i–k) Reproduced with permission.[231] Copyright 2022, Wiley-VCH.

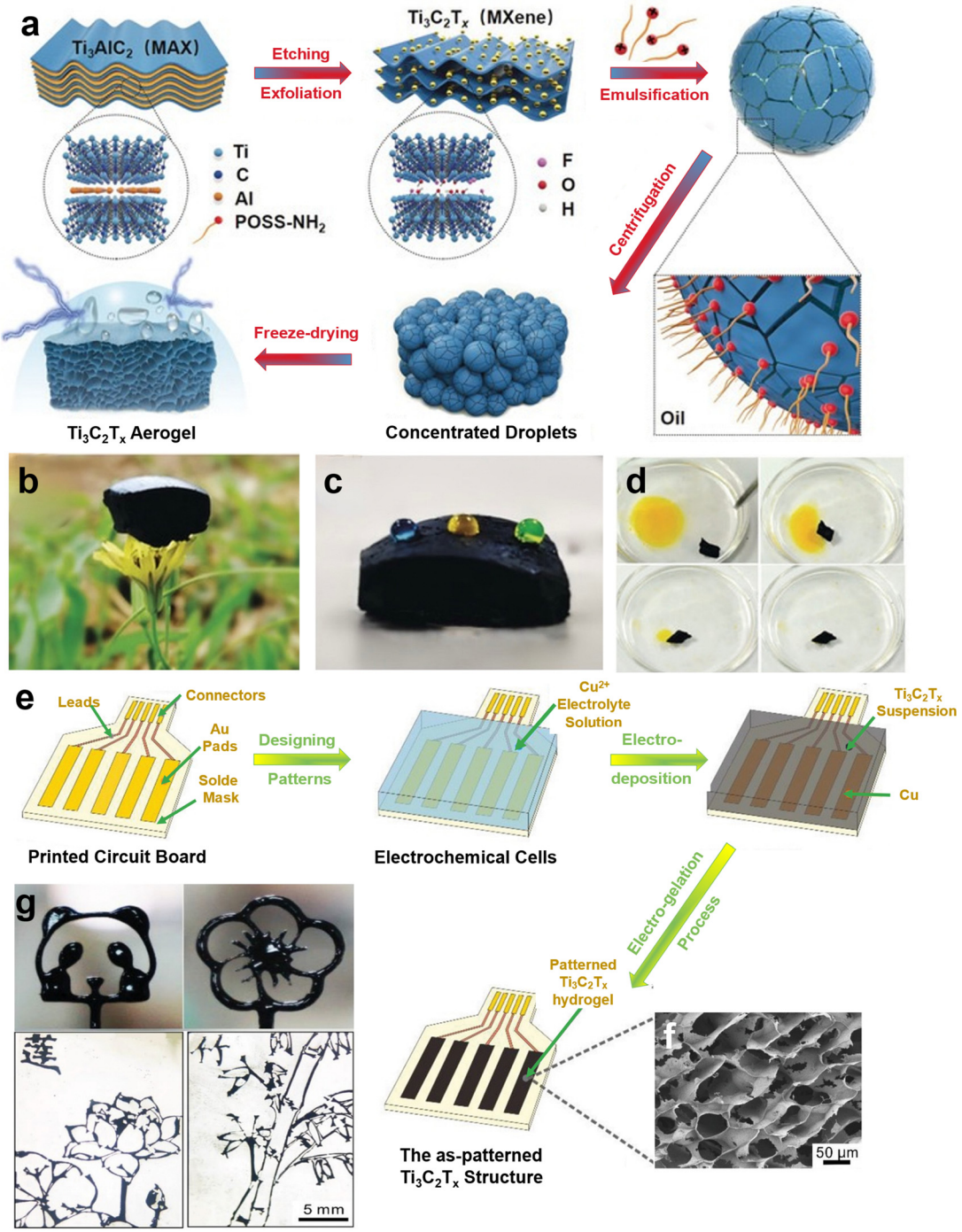

Fig. 4 (a) Schematic illustration of interfacial co-assembly and jamming of $Ti_3C_2T_x$ and POSS-NH_2 at the toluene/water interface. The prepared structured liquids were used as a template for aerogel fabrication. (b–d) The prepared aerogels showcased exceptionally low density, hydrophilic nature with a water contact angle of 123°, and unique oil absorption characteristics. The yellow oil phase in (d) is *n*-hexene dissolving azobenzene. (a–d) Reproduced with permission.[235] Copyright 2019, Wiley-VCH. (e) Schematic of the metal ionic cross-linking technique for producing well-patterned MXene hydrogels/aerogels. (f) The SEM image of patterned $Ti_3C_2T_x$ structure. (g) The proposed metal ionic cross-linking approach is capable of fabricating complex geometries, which are hard to achieve through other processing techniques. (e–g) Reproduced with permission.[236] Copyright 2021, Wiley-VCH.

and catalysts.[245–253] For instance, Xu *et al.*[254] developed double-negative-index h-BN/graphene ceramic aerogels for thermal superinsulation under extreme conditions with ultra-low density down to ~0.1 mg cm^{-3} (Fig. 5e). In brief, they fabricated graphene-based aerogels with hyperbolic architecture *via* a modified hydrothermal reduction and noncontact freeze-drying approach as a template. The attained porous aerogels were then used as templates to obtain h-BN aerogels through

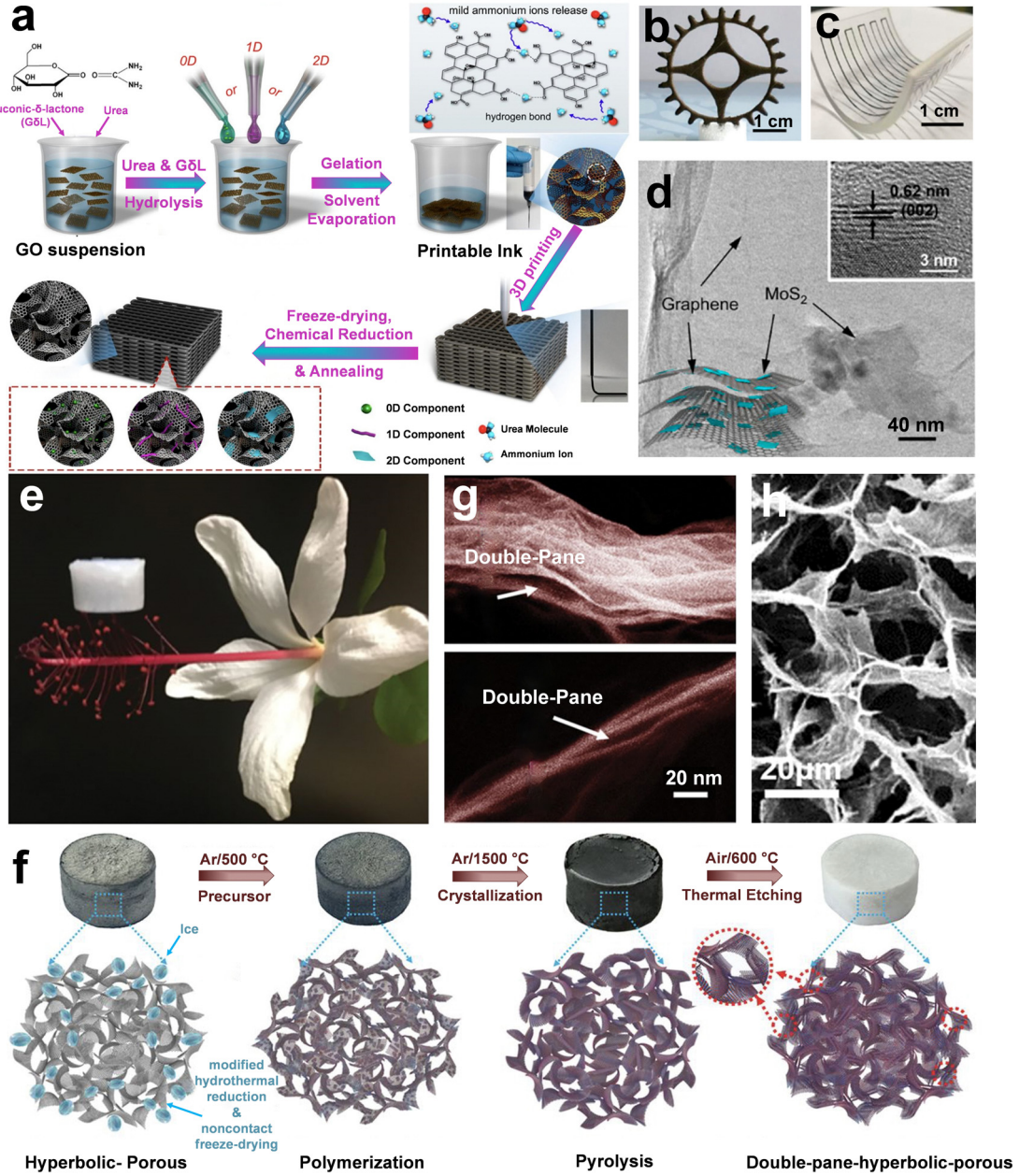

Fig. 5 (a) Schematic illustration of ink fabrication and 3D printing of mixed-dimensional hybrid inks. (b) Optical image of a 3D-printed aerogel of GO with a toothed gear pattern. (c) A nonplanar geometry is prepared by printing MoS_2/GO hybrid ink. (d) The transmission electron microscopy (TEM) confirmed the bounding of MoS_2 in the cross-linked GO nanosheets. (a–d) Reproduced with permission.[244] Copyright 2018, American Chemical Society. (e) The optical image of ultra-light h-BN aerogel resting on the stamen of a flower. (f) Schematic illustration of ultra-light h-BN aerogel fabrication through chemical vapor deposition of borazine on graphene aerogel template followed by thermal etching of graphene skeleton. (g and h) SEM images of the corresponding aerogel demonstrate (g) the double-pane wall structure caused by the thermal etching of graphene templates and (h) the microstructure of the h-BN aerogel. (e–h) Reproduced with permission.[254] Copyright 2019, The American Association for the Advancement of Science.

chemical vapor deposition of borazine. Borazine was first self-condensed into polyborazylene and then polymerized into amorphous BN coating on a graphene aerogel template *via* dehydrogenation at 500 °C. Upon further annealing at 1500 °C, the amorphous BN crystalized into the highly ordered h-BN. Finally, the hybrid was annealed in air at 600 °C to etch the graphene template (Fig. 5f). Thermal etching of graphene templates formed a double-pane wall structure for h-BN aerogels. Benefiting from the high bending stiffness of h-BN, the face-to-face collapse of these constructs was prevented, and the average gap size between the double-pane walls was controlled from a few to tens of nanometers (Fig. 5g and h). The corresponding h-BN aerogels exhibited exceptional mechanical and thermal characteristics with a negative Poisson's ratio of −0.25 and a negative linear thermal expansion coefficient of -1.8×10^{-6} °C. Furthermore, an elasticity of up to 95%, near-zero strength loss after sharp

thermal shocks, and ultra-low thermal conductivity in the vacuum of ~20 mW m^{-1} K^{-1} were observed for this class of ceramic aerogels.

4. The marriage of 2D nanomaterial-based aerogels and PCMs

Encapsulating PCMs into multiscale supporting materials, also known as PCM confinement, revolutionized the development of multifunctional yet shape-stabilized thermal management systems.[83,84,255] Depending on the dimensions of the supporting materials, confinement strategies are categorized into four subclasses, including core–shell (0D), longitudinal (1D), interface (2D), and porous (3D) confinements.[89] 0D confinement is defined as encapsulating PCMs with a protective layer through a core–shell structure, while 1D confinement is based on embedding PCMs into the inner cavity of nanofibrous materials such as CNTs. It is also possible to lock PCMs between the layers of various 2D nanomaterials, *e.g.*, graphene, MXene, and h-BN, through the interfacial interaction of the nanoparticles' surface and PCM molecules. Finally, in 3D confinement, aerogels are used as a template or holder to host PCMs in the interconnected nanoporous framework.[89] Aerogel confinement is proven to be one of the most effective ways to control the leakage of PCMs.[89] Besides, composite PCMs can inherit the inherent characteristics of their host and gain a second functionality (see Table 3 and the corresponding discussions in Sections 4-1 to 4-3). For example, composite PCMs of graphene or MXene can simultaneously showcase high electrical conductivity and unique thermal management characteristics, opening up numerous applications ranging from thermal management to EMI shielding.[256–260]

4.1. Graphene-based composite PCMs

Graphene-based aerogels, widely considered supporting materials, are a milestone in versatile advanced multifunctional composite PCMs with a higher thermal conductivity than pure PCMs. For example, Ye *et al.*[261] developed core–shell-like structured graphene/paraffin composite PCMs through a modified hydrothermal method. First, cyclohexane as a paraffin solvent was mixed to GO aqueous suspension to form a stable and homogenous graphene/paraffin emulsion. Next, graphene gels with micron-sized cyclohexane/paraffin droplet fillings were obtained after sequentially sealing the emulsion in Teflon autoclaves and heating it to 160 °C. The graphene-wrapped-cyclohexane hydrogels were then immersed in deionized water to remove the paraffin solvent and freeze-dried to fabricate a shape-stable composite PCM. The resultant composites are considered promising candidates for thermal energy storage systems, presenting an increase of 32% over the thermal conductivity of pure paraffin with a high paraffin encapsulation of 97 wt%, high enthalpy of 202.2 J g^{-1}, and freezing enthalpy of 213 J g^{-1}.

In another study, Wang *et al.*[262] introduced a programmable method to shape graphene/paraffin composites efficiently. In this regard, the ink-jetting coupled with liquid marbling and supercritical fluid drying approaches were used to develop monodispersed graphene beads (Fig. 6a). Initially, uniform sol–gel droplets of GO/vitamin C with a narrow size distribution were fabricated through ink-jetting. Liquid marbling technology was then used to suppress the amalgamation and collision of the graphene-based droplets. Finally, the aerogel beads were prepared through CO_2 supercritical drying. A novel graphene-based composite PCM was obtained by capillary filling the aerogel beads with paraffin. The crystallinity, high latent heat, and high stability of PCMs were well maintained through these structures due to the existence of micro/nanopore channels of microsphere aerogels (Fig. 6b and c).

Interestingly, these micro-sphere composite PCMs were adopted into micro-circuits and were used as ultra-sensitive heat sensors with a detection limit of as low as 0.027 J. In a similar study, GO aerogel beads were developed through wet-spinning self-assembly of GO suspension into a coagulation bath containing 1 wt% polyethyleneimine (PEI) aqueous solution. The obtained graphene-based aerogel provided capillary forces and infiltration pathways for the impregnation of 1-tetradecanol (1-TD), *i.e.*, chemically pure paraffin. GO droplets were formed by extruding GO aqueous slurry *via* a syringe needle into a coagulation bath (Fig. 6d). The fabricated wet beads were then rinsed with deionized water, freeze-dried, and annealed at 110 °C to acquire reduced graphene beads (Fig. 6e and f). Finally, a composite PCM with a high latent heat of 232.2 J g^{-1} was achieved by soaking the reduced aerogels in 1-TD. The thermal responsive tests of these composite PCMs before and after reduction are presented in Fig. 6g.[263]

Typically, the thermal conductivity of composite PCMs is expected to be amplified due to the PCM confinement. However, the considerable interfacial thermal resistance between graphene-based aerogels and PCMs can adversely affect the thermal conductivity of composite PCMs. In order to address this challenge, Mu and Li[264] fabricated surface-modified graphene-based aerogels to diminish the interfacial thermal resistance between aerogels and PCMs. After adding vitamin C and/or EDA to the GO aqueous solution, a hydrogel was attained and freeze-dried to fabricate surface-modified graphene aerogel. Then, functionalized composite PCMs were obtained by infiltrating TD into the graphene/EDA and graphene/vitamin C interconnected network. Due to the uniform distribution of TD, the fabricated composite PCMs showcased unique stability with minimum PCM leakage.

High-temperature thermal annealing is another versatile approach to enhance the thermal conductivity of graphene-based composite PCMs without compromising the aerogels' features. For instance, Yang *et al.*[62] developed a densely packed graphene aerogel by freeze-drying the molded GO paste with various architectures and annealing at 2800 °C. The fabricated aerogels were then infiltrated with 1-octadecanol (1-OC) to obtain shape-stable composite PCMs, even under simultaneous compressive force and thermal heating at 70 °C. Compared to the pristine PCM, the thermal conductivity and the latent heat of the as-made composite PCM enhanced up to 4.28 W m^{-1} K^{-1} (1760% higher than that of pure 1-OC) and ~225 J g^{-1}, respectively.

Despite the progress discussed earlier with regard to graphene-based composite PCMs, their rigidity still hinders their potential for use in the thermal management of smart

Table 3 A library on 2D nanomaterial-based composite PCMs: form aerogel fabrication to thermal characteristics and adopted applications

			PCM/aerogel composite							
Aerogel material	Aerogel fabrication process	Type of PCMs	PCM loading (wt%)	K_m[a] (W m^{-1} K^{-1})	K_c[b] (W m^{-1} K^{-1})	η[c] (%)	T_m/T_f[d] (°C)	$\Delta H_m/\Delta H_f$[e] (J g^{-1})	Functionality	Ref.
rGO/expanded graphite	Hydrothermal reduction Freeze-drying	Paraffin wax	92.42	0.2	0.79	295	52.9/46.2	210.6/207.2	Light-thermal energy storage	288
rGO/PAAS	Directional freeze-casting Freeze-drying Thermal annealing	Paraffin wax	—	0.35	8.87/2.68	2434/665	—	179.0/—	Solar-thermal energy conversion	289
rGO	Emulsification Chemical reduction Freeze-drying	Paraffin wax	97	0.207	0.274	32	41.0/58.0	202.2/213.0	Thermal energy storage	261
rGO/CNTs	Hydrothermal reduction Freeze-drying	Paraffin wax	97.8	0.207	0.46	77	50.8/45.8	121.0/116.9	Solar-thermal energy conversion	290
rGO/CNTs	Chemical-induced gelation Freeze-drying	Paraffin wax	98.15	0.2	0.836	318	46.6/—	245.5/—	Thermal management	291
rGO	Wet-spinning Freeze-drying Thermal annealing	1-TD paraffin	99.83	—	—	—	40.0/—	232.2/228.4	Thermal energy storage Thermal management	263
rGO	Chemical-induced gelation Freeze-drying Thermal annealing	*n*-Octadecane	96.7	0.15	0.47	215	35.1/13.8	195.7/196.7	Thermal energy storage	292
rGO/graphene nano-plates (GNPs)	Freeze-drying	PEG 10 000	97.75	0.31	1.43	361	64.8/41.8	185.6/177.8	Light-thermal energy conversion Energy storage	293
rGO/CNTs	Chemical-induced gelation Freeze-drying	PEG 2000	98.79	0.227	0.76	235	53.8/—	162.2/—	Thermal management	294
rGO/lignin	Chemical-induced gelation Freeze-drying	PEG 4000	99.2	—	0.384	—	61.0/42.0	168.7/165.1	Solar-thermal energy conversion	295
GO	Cross-linking Freeze-drying	PEG 6000	99.5	0.211	0.344	63	42.0/61.0	218.9/213.2	Thermal energy storage	296
rGO/GNPs	Hydrothermal reduction Air-drying Thermal annealing	1-OC	86.7	0.21	9.5	4423	62.0/48.53	196.2/234.1	Solar-thermal energy conversion Energy storage	297
rGO/GNPs	Hydrothermal reduction Air-drying	1-OC	88	0.23	5.92	2473	59.0/53.9, 49.3	202.8/250.8	Thermal management Insulation	298
rGO	Freeze-drying Thermal annealing	1-OC	95	0.23	4.28	1761	61.0/53.9	225.3/289.0	Thermal energy storage	62
rGO	Chemical-induced gelation Freeze-drying	Lauric acid	94.31	0.267	1.207	352	43.3/40.6	207.3/205.8	Solar-thermal energy conversion Energy storage	299
Carbonized GNPs/CNFs/melamine foam	Directional freeze-casting Freeze-drying Thermal annealing and carbonization	Paraffin wax	95.9	0.28	1.42	407	52.4/46.3	154.3/159.7	Solar-thermal energy conversion Electronic-thermal energy storage	300
rGO/TiO_{2-x}	Chemical-induced gelation Freeze-drying	Paraffin wax	92.4	0.35	1.22	248	55.7/50.4	127.8/128.5	Photo-thermal conversion	301
rGO/GNPs	Chemical vapor deposition of graphene on Ni/rGO foam	Paraffin wax	—	0.27	1.82	574	57.3/47.6	145.2/139.2	Light-thermal energy conversion Energy storage	302
rGO/Cu foam	Chemical Reduction	Paraffin wax	94.81	0.3	3.0	900	45.6/—	133.6/—	Solar energy conversion	303

Table 3 (*continued*)

Aerogel material	Aerogel fabrication process	Type of PCMs	PCM/aerogel composite: PCM loading (wt%)	K_m[a] (W m^{-1} K^{-1})	K_c[b] (W m^{-1} K^{-1})	η[c] (%)	T_m/T_f[d] (°C)	$\Delta H_m/\Delta H_f$[e] (J g^{-1})	Functionality	Ref.
	Freeze-drying								Energy storage	
rGO/poly(ethylene glycol)-grafted cellulose	Freeze-drying Chemical reduction	PEG 6000	—	0.272	0.761	180	68.8/35.9	185.5/170.3	Thermal energy storage	304
rGO	Chemical-induced gelation Freeze-drying	Methoxy poly(ethylene glycol) mono-methacrylate (*m*-PEGMA)	—	—	—	—	58.7/27.3	177.0/176.0	Solar-thermal-electric energy conversion	305
rGO/GNPs	Freeze-drying	1-TD	—	—	0.4069	—	42.87/30.3	213.7/212.4	Electrothermal energy harvesting	306
rGO/GNPs	Freeze-drying Chemical reduction	1-TD	—	0.0812	0.3408	320	44.68	220.4/213.6	Electrothermal energy harvesting	307
rGO	Ink jetting Liquid marbling Supercritical drying	Paraffin wax	91.3	—	—	—	47.8/—	136.6/144.4	Thermal Buffers Microelectronic devices	262
rGO/h-BN	BDFC Freeze-drying Thermal annealing	PEG 10 000	88.35	0.3	2.94	880	—	145.5/—	Solar-thermal-electric energy conversion	281
rGO	Chemical-induced gelation Freeze-drying	1-TD	90	0.221	1.092	394	35.4/34.1	177.7/180.2	Thermal energy storage	264
rGO/konjac glucomannan	Chemical-induced gelation Freeze-drying Deacetylation	Sodium acetate trihydrate (SAT)	—	—	—	—	57.8/—	230.3/230.3	Solar-thermal energy conversion Energy storage	308
rGO/PVA/MMT nanosheets	Freeze-drying	Lauric acid	98.5	0.267	0.418	57	42.3/40.3	191.2/192.2	Solar-thermal energy conversion	309
rGO	Chemical-induced gelation Supercritical drying	Paraffin wax	94.8	—	—	—	—	—	Thermal energy storage	310
GNPs/cellulose	Chemical-induced gelation Freeze-drying	PEG 6000	89.2	—	1.35	—	63.0/44.3	156.1/148.9	Thermal energy storage	311
rGO/BN nanotube	Chemical-induced gelation Freeze-drying	PEG 4000	98.5	0.29	0.43	48	59.1/38.5	195.6/175.9	Thermal management	312
rGO/scaphium scaphigerum	Chemical-induced gelation Freeze-drying	PEG 4000	—	0.28	1.15	311	63.0/43.8	164.2/140.6	Energy storage	313
rGO/CNTs	Freeze-drying Thermal annealing	Paraffin	98	0.2	2.182	991	48.1/—	222.1/—	—	314
rGO/BN	Chemical-induced gelation Freeze-drying Microwave reduction	Paraffin	82.5	0.2782	1.68	504	54.1/47.4	123/—	Thermal energy storage Solar energy conversion	315
Graphite nanosheet/gelatin	Freeze-casting Freeze-drying	Paraffin	>93.2	0.264	3.75	1320	59.8/41.7	146.4/153.7	Building energy saving Human body hyperthermia Solar energy collection system	316
rGO/cellulose nanocrystals	Chemical-induced gelation Freeze-thawing Chemical reduction Air-drying	PEG 6000	—	0.213	0.443	108	64.9/35.0	183.2/165.9	Energy storage	317
rGO/BN/melamine foam	Chemical reduction Freeze-drying	PEG 6000	93.24	0.30	0.79	163	63.5/34.7	160.7/145.1	Thermal management component	318

Table 3 (*continued*)

Aerogel material	Aerogel fabrication process	Type of PCMs	PCM/aerogel composite: PCM loading (wt%)	K_m[a] (W m^{-1} K^{-1})	K_c[b] (W m^{-1} K^{-1})	η[c] (%)	T_m/T_f[d] (°C)	$\Delta H_m/\Delta H_f$[e] (J g^{-1})	Functionality	Ref.
									Thermoelectric devices under emergency conditions	
$Ti_3C_2T_x$/gelatin	Freeze-drying	Paraffin wax	97.7	0.26	0.92	248	60.1/38.3	191.7/192.9	Solar-thermal energy storage	319
$Ti_3C_2T_x$	Freeze-drying	PEG 4000	95	—	—	—	57.5/33.8	112.3/108.5	Solar energy conversion Energy storage	267
$Ti_3C_2T_x$	Freeze-drying	Phosphorus-modified stearyl alcohol	80	0.353	0.486	37	79.2/50.7	120.1/122.7	Thermal insulation Solar-thermal energy storage	266
$Ti_3C_2T_x$/polyimide	Freeze-drying	PEG 10 000	97.68	0.2109	0.3533	68	62.45/—	177.1/173.5	Solar-thermal energy conversion Energy storage	269
$Ti_3C_2T_x$/bacterial cellulose	Freeze-drying Chemical vapor deposition of MTMS	Paraffin wax	88.56	—	—	—	23.42/19.2	89.02/93.49	Photo-thermal energy conversion Energy storage	273
$Ti_3C_2T_x$/bacterial cellulose	Freeze-drying	PEG 4000	97.9	—	—	—	67.0/41.5	196.7/191.7	Photo-thermal conversion Energy storage	320
Dopamin functionalized $Ti_3C_2T_x$/CNFs	Chemical-induced gelation Freeze-drying	Erythritol	—	0.27	0.465	72	125.3/63.5	330.6/309.8	Solar-thermal-electric energy conversion	268
$Ti_3C_2T_x$/Ni-platted/melamine spong/GNPs/CNFs	Freeze-drying Vacuum-assisted filtration	PEG 6000	99.61	0.27	0.48	78	63.0/38.9	154.3/150.3	EMI shield Thermal management	321
$Ti_3C_2T_x$/poly(3,4-ethylenedioxythiophene) polystyrene sulfonate (PEDOT:PSS)	Freeze-casting Freeze-drying	PEG 20 000	98.78	0.3	0.36	20	61.6/46.9	237.6/236.1	EMI shield Thermal management	322
h-BN/CNFs	Freeze-drying	PEG 10 000	90	0.33	4.764	1344	60.2/41.6	136.8/122.8	Thermal insulation Solar-thermal energy storage	323
L-Glutamine grafted h-BN/CNFs	Chemical-induced gelation Freeze-drying	PEG 1500	—	0.28	0.59	110	42.3/15.2	143.5/136.1	Thermal energy storage	280
h-BN/CNFs/Polyethylenimine (PEI)	Chemical-induced gelation Freeze-drying	PEG 6000	95.6	0.28	0.4	43	57.2/34.2	165.3/169.3	Electric-thermal management	324
MoS_2/MMT	Freeze-drying	Paraffin wax	—	—	—	—	41.3/43.4	151.7/145.8	Solar desalination Freshwater production	285
h-BN/chitosan	Freeze-drying	Paraffin wax	59	0.28	1.14	307	50.5/52.9	118.4/114.9	Electric-thermal energy storage	282
Biomass carbon	Freeze-drying Pyrolysis	Paraffin wax	95	0.248	0.427	72	63.5/54.5	83.6/98.8	Light-thermal energy conversion Energy storage	325

[a] Thermal conductivity of PCM. [b] Thermal conductivity of aerogel-based composite PCM. [c] $\frac{k_{aerogel/PCM} - k_{PCM}}{k_{PCM}}$. [d] Melting temperature/freezing temperature. [e] Melting latent heat/freezing latent heat.

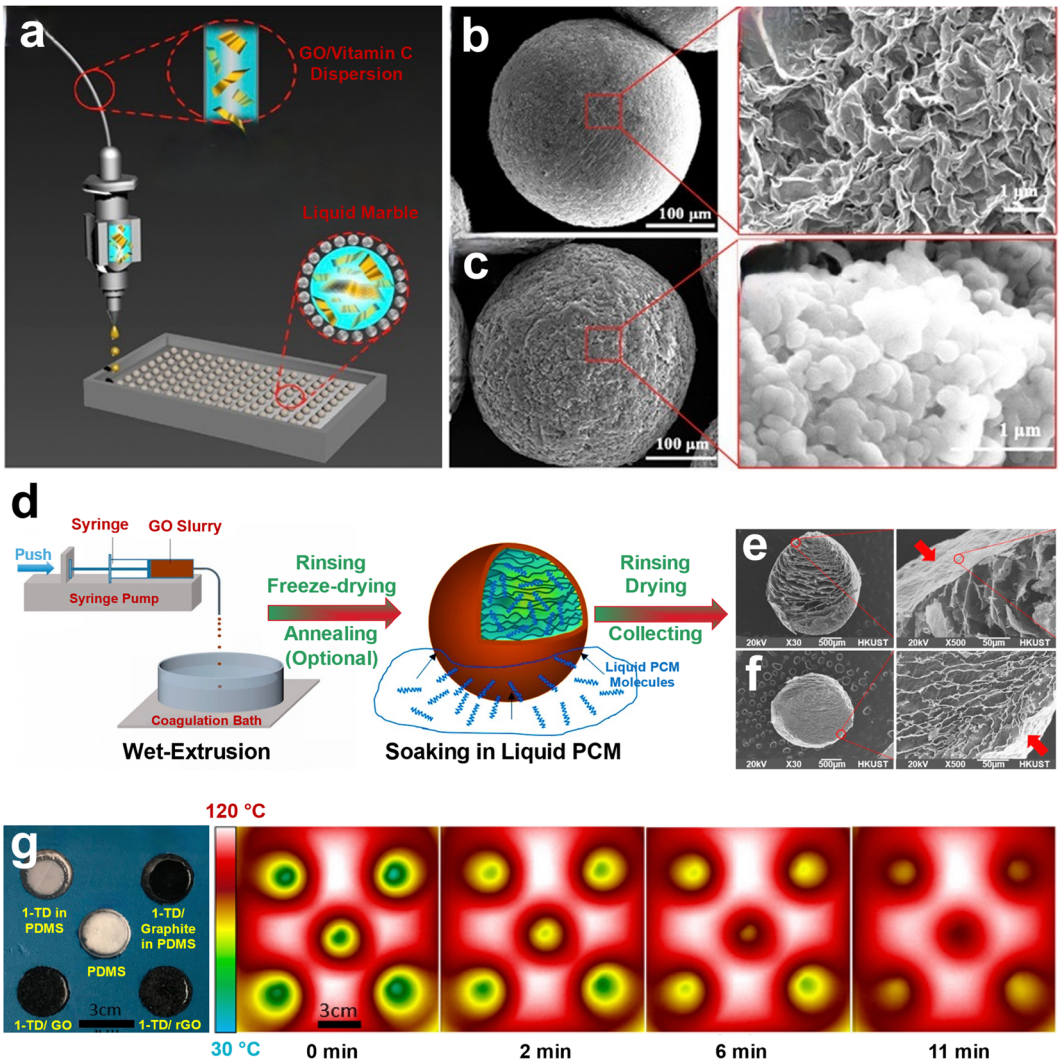

Fig. 6 (a) Schematic illustration of monodispersed graphene beads fabrication through ink-jetting coupled with liquid marbling and supercritical fluid drying. (b and c) SEM images of the fabricated (b) graphene-based aerogel microspheres and (c) the corresponding graphene/paraffin composites. (a–c) Reproduced with permission.[262] Copyright 2017, American Chemical Society (d) Schematic illustration of GO/1-TD composite PCM fabrication. (e and f) SEM images of (e) neat graphene beads and (f) the corresponding GO/1-TD composite PCMs. (g) Infrared thermal images of PDMS, 1-TD in PDMS, 1-TD/graphite in PDMS, 1-TD/GO, and 1-TD/rGO were placed on a hot plate. (d–g) Reproduced with permission.[263] Copyright 2019, American Chemical Society.

flexible devices. To address this challenge, Sun *et al.*[99] have developed a novel flexible graphene/polyvinylidene fluoride-hexafluoropropylene (PVDF-HFP) aerogel-based composite phase change film. By introducing PVDF-HFP, the porous framework of graphene aerogel is strengthened, resulting in a superior flexible aerogel. Paraffin wax was impregnated into the supporting matrix to obtain the final phase change composite aerogels. The developed composite exhibited excellent thermal properties, long-term cycle stability, advanced flexibility, and outstanding solar-thermal conversion ability. The phase change enthalpy of this composite PCM reached 154.64 J g^{-1} and remained stable even after 500 heating–cooling cycles. The solar-thermal conversion efficiency of the developed composite PCMs was evaluated to be 95.98%, indicating a superior ability to convert solar energy into thermal energy. Interestingly, this flexible graphene-based composite PCM was attached to a human model to demonstrate its advanced performance of wearable thermal management. Moreover, the excellent thermal energy storage capacity and solar-thermal conversion ability enable the graphene-based composite PCM to capture thermal heat from diverse energy sources. Therefore, this composite PCM has promising potential for broadening the application scenarios of advanced thermal energy management, not only for the intelligent temperature control equipment of the human body, but also for the thermal management of other complicated surfaces on controlled devices.

Shi *et al.*[100] also researched the development of mechanically robust and foldable graphene-based composite PCMs. To this end, the authors synthesized polyimide/graphene/Fe_3O_4 hybrid aerogel films through a series of steps, including pre-polymerization, film

casting, freeze-drying, and thermal imidization. Subsequently, the researchers impregnated the aerogel framework with PEG as a PCM under a vacuum condition. The resulting hybrid aerogel films possessed ultra-light, foldable, and flexible characteristics. Furthermore, the hybrid aerogel films exhibited a high PEG loading of nearly 90 wt% due to their macroporous structure and large pore volume. The resultant hybrid aerogel/PEG composite films possessed good thermal management capability to regulate temperature through thermal energy absorption and release under a latent-heat capacity of over 158 J g^{-1}. More importantly, the multifunctional composite films displayed a wideband absorption capability at 7.0–16.5 GHz and a minimum reflection loss of −38.5 dB, resulting in excellent EM and infrared bi-stealth performance through the effective wideband microwave absorption of graphene/Fe_3O_4 component and the thermal buffer of PEG.

4.2. MXene-based composite PCMs

MXene-based aerogels are fascinating supports for composite PCMs due to their exceptional electrical conductivity, high photothermal energy conversion efficiency, and acceptable thermal conductivity.[89,265,266] Lin *et al.*[267] introduced a sustainable and environmentally friendly fabrication strategy to establish MXene-based composite PCMs for solar-thermal energy management. In this work, MXene skeleton is considered a photothermal agent with high extinction coefficients in the ultraviolet-visible-near-infrared (UV-Vis-NIR) region, while PEG with high affinity to $Ti_3C_2T_x$ acts as a medium for thermal energy storage. The homogeneous $Ti_3C_2T_x$/PEG dispersion was obtained by stirring, sealing, and heating the mixture of the PEG solution and $Ti_3C_2T_x$ colloid. Upon one-step freeze-drying, a binary $Ti_3C_2T_x$-based composite PCM was fabricated, possessing a density of 30 mg cm^{-3} and a solar-thermal conversion efficiency of 92.5%.

In another study, Du *et al.*[268] fabricated a novel biomass-derived composite PCM by impregnating sugar alcohol PCMs into MXene/CNFs aerogels. Selectively etching an aluminum layer of Ti_3AlC_2 followed by self-polymerization of dopamine on $Ti_3C_2T_x$ resulted in synthesizing 2D-layered polymerized dopamine-decorated nanosheets. A porous network was produced by sequential cation-induced gelation of the MXene/CNFs suspension and subsequent freeze-drying of the obtained hydrogel. The consequent aerogel loaded with erythritol, *i.e.*, sugar alcohol PCMs, to achieve a form-stable composite PCM offering solar-thermal-electricity conversion capacity with a maximum output voltage of 0.63 V. MXene-based composite PCMs were also used for solar-driven seawater desalination. First, as a water-soluble polyimide precursor, poly(amic acid) ammonium salt (PAAS) was synthesized through a polycondensation reaction. Then, by successive chemical reduction, freeze-drying, and thermal annealing, MXene/polyimide aerogels were fabricated and loaded with a high content of PEG, *i.e.*, up to 97.68 wt%. The as-fabricated composite PCMs exhibited a high enthalpy efficiency of up to 95.16%, an exceptional seawater evaporation mass of 6.07 kg m^{-2}, a high evaporation rate of 1.24 kg m^{-2} h^{-1} under one-sun illumination, and a high evaporation efficiency of 50.6%.[269]

A flame-retardant MXene-based composite PCM with high thermal stability was designed based on the chemical modification of stearyl alcohol (SAL) with a phosphorus-containing molecule. In this strategy, the MXene-based supporting skeleton was fabricated by freeze-casting and subsequent freeze-drying of $Ti_3C_2T_x$ suspensions. The flame-retardant composite PCMs were then made by a facile vacuum impregnation into the $Ti_3C_2T_x$ aerogels to hinder the PCM leakage. These flame-retardant and form-stable composite PCMs with a high thermal conductivity of 0.486 W m^{-1} K^{-1} PCM can potentially be used for solar energy storage applications.[266]

In another study, Cao *et al.*[101] developed a multifunctional MXene-based composite PCM that exhibits excellent EMI shielding and efficient thermal energy management capabilities. This was achieved through the hybridization of cellulose nanocrystal/konjac glucomannan with intrinsically conductive $Ti_3C_2T_x$ nanosheets, followed by freeze-drying and thermal annealing. The resulting aerogels were then filled with paraffin wax using a vacuum impregnation method, which produced the aerogel-based phase change composites. The fabricated constructs exhibited notable reusable stabilities, excellent EMI shielding properties, and efficient thermal energy management capacities. For instance, the composite containing 2.3 wt% of $Ti_3C_2T_x$ demonstrated exceptional solar-thermal and electro-thermal conversion capabilities. Additionally, the EMI shielding effectiveness value was recorded at 45.0 dB (blocking more than 99.99% of unwanted electromagnetic noises), with a corresponding melting enthalpy value of 215.7 J g^{-1} (relative enthalpy efficiency of 99.9%). These findings suggest that the fabricated composite PCMs hold great potential for packaging sensitive electronics in the field of military and medical applications, due to their outstanding EMI shielding and advanced thermal energy management capabilities.[270,271]

MXene-based composite PCMs have also been used as a promising solution for dual-camouflage under infrared/visible bands. To this end, Li *et al.*[272] have fabricated a trilayer composite that integrates key features such as thermal insulation, heat absorption, solar/electro-thermal conversions, and thermochromism. This innovative composite consists of an anisotropic $Ti_3C_2T_x$/rGO hybrid aerogel, with n-octadecane PCM at the bottom and a thermochromic coating on the upper surface. By leveraging the heat insulation of the porous aerogel and the heat absorption capabilities of the PCM, the composite significantly minimizes the temperature difference between the human target and its surroundings to 0.9 °C, providing infrared-stealth ability in low-temperature environments such as jungles and night conditions. Furthermore, it can conceal low-temperature object signals in the infrared image of high-temperature backgrounds and can be molded into a fake humanoid target with presupposed infrared characteristics to interfere with infrared detection. In addition, the composite adapts to varying environments by spontaneously increasing its surface temperature *via* solar-thermal conversion to around 50 °C, thus altering its color from green to yellow in 30 seconds to match the ambient infrared characteristic and blend with the surrounding sandy color. This versatile and environmentally adaptable camouflage design holds

great promise for applications in daily thermal management and military protection.

In another intriguing study inspired by the smart thermal management of antifreeze beetles, Ji *et al.*[273] devised composite PCM films by impregnating paraffin in a surface-modified MXene/bacterial-cellulose aerogel (Fig. 7). Antifreeze beetles have been blessed with a synergistic thermal regulation stemming from the light absorption of the black surfaces and the proteins' energy storage capability. In order to mimic this thermal management behavior of antifreeze beetles, MXene/bacterial-cellulose hybrid aerogels were fabricated by freeze-drying the suspension of the exfoliated $Ti_3C_2T_x$ and bacterial-cellulose. The surface of the prepared aerogels was then modified through hydrophobic groups *via* chemical vapor deposition of methyltrimethoxysilane (MTMS). This surface modification approach not only strengthened the interaction between aerogel and PCMs but also prevented the leakage of liquid paraffin. Through forging and vacuum impregnation of PCMs into hydrophobic MXene-based

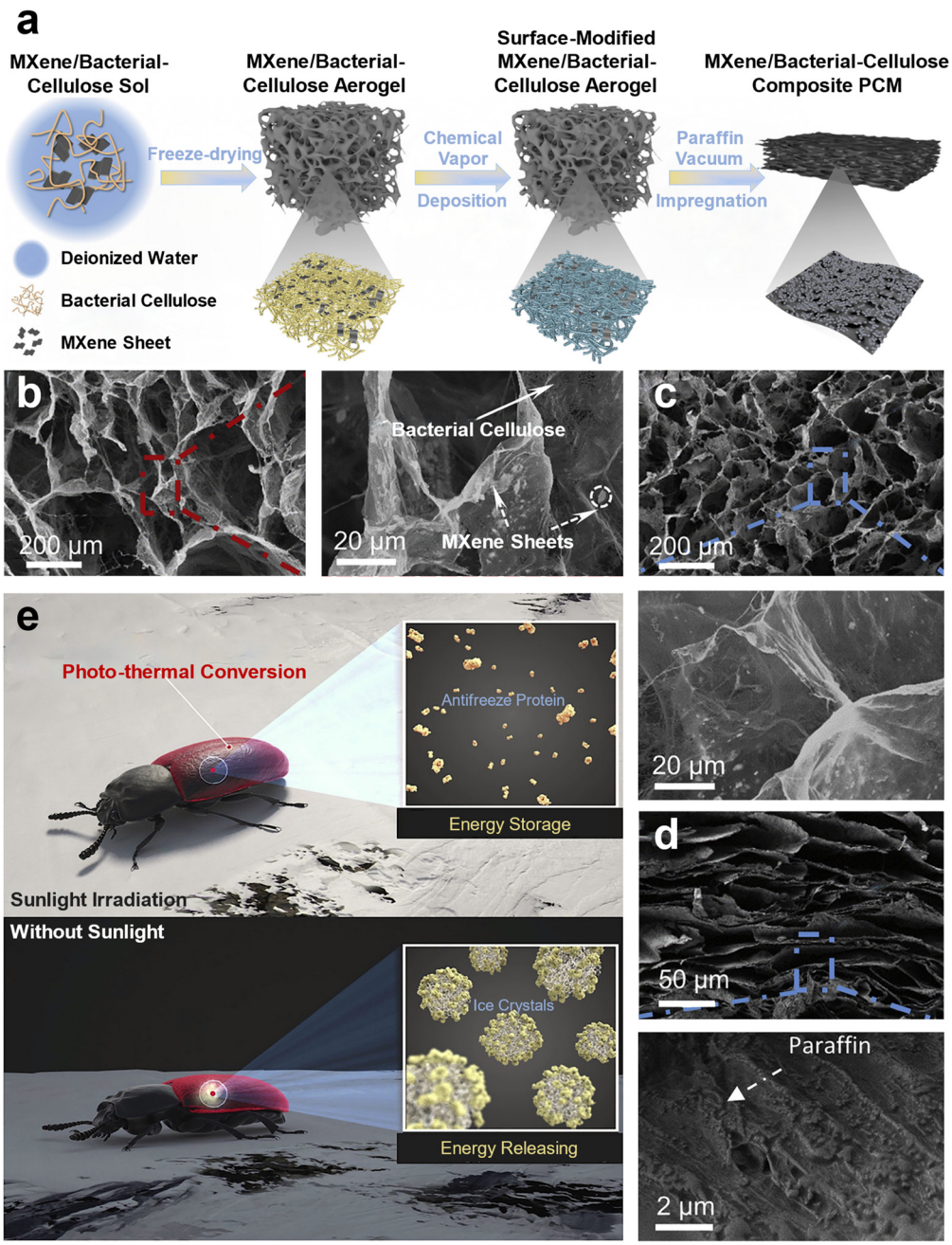

Fig. 7 (a) The preparation process of a surface-modified MXene/bacterial-cellulose aerogel-based composite PCM. (b–d) SEM images of (b) MXene/bacterial-cellulose aerogel, (c) the corresponding composite PCM, and (d) surface-modified MXene/bacterial-cellulose aerogel-based composite PCM. (e) Antifreeze beetles absorb sunlight energy through black spots and antifreeze proteins on their skins. This thermal energy will be released at night or in cold weather. Reproduced according to the terms of the Creative Commons CC-BY-NC-ND license.[273] Copyright 2022, Elsevier.

supports, the MXene/bacterial-cellulose composite PCMs with super-lipophilic features were achieved. Finally, composite PCMs were compressed by a 5 kg weight to attain compact and laminated structures. Interestingly, the photothermal conversion of MXenes mimicked the black surface of beetles, while thermal storage through crystallization of PCMs resembled the energy storage of antifreeze proteins, resulting in bio-inspired thermal management systems.

4.3. Other 2D materials composite PCMs

Although a rapid heat transfer throughout composite PCMs is accomplished by adopting a highly thermally conductive network of either graphene-based or MXene-based aerogels, this concept could be applicable to aerogel-based composite PCMs of other 2D materials. The h-BN, so-called ''white graphite'', with a similar structure to graphite, states high thermal conductivity, excellent electrical insulation properties, high thermal stability, and oxidation resistance, and therefore, has been used for developing advanced composite PCMs.[274–279] For instance, a functionalized h-BN/CNFs composite PCM was reported to have 4.5 times higher thermal diffusivity than a pristine PEG, a high phase change enthalpy of 150.1 J g^{-1}, and excellent shape stability. In this work, an in-situ process was employed to functionalize h-BN nanosheets with hydroxyl and amino groups through ball-milling a mixture of L-gluutamine and h-BN for 24 h. The L-gluutamine-grafted h-BN/CNFs hydrogel was then formed by adding CNFs as the cross-linking agent to the suspension. The as-prepared hydrogel was freeze-dried to construct a robust and porous aerogel, which was then applied as a PEG 1500 confinement.[280]

The integration of h-BN composite PCMs with solar-thermoelectric generators was used to develop long-lasting energy generation systems for storing and converting clean solar energy. In this regard, a biomimetic aerogel of h-BN/GO, resembling the water-transportation microstructure of elaborate conifer trees, was designed through BDFC and used as a supporting skeleton for composite PCMs (Fig. 8a–f). The vacuum impregnation of 88.35 wt% PEG into these centrosymmetric and radially aligned aerogels led to the formation of high-performance composite PCMs for durable and real-environment solar-to-thermal/electric conversion with an effective photothermal energy conversion of ~85.1%, an enhanced thermal conductivity of 880% over the thermal conductivity of pure PEG, and a high peak power density of 40.28 W m^2.[281]

Du *et al.*[282] also focused on degradable composite aerogels of h-BN as a substrate for stabilizing PCMs. The h-BN/chitosan suspensions were prepared by dispersing h-BN nanosheets in chitosan/acetic acid solution and poured into a Teflon mold. The resulting suspension was then freeze-dried to achieve a 3D aerogel framework with a well-preserved micro-structure. These aerogel templates were finally submerged into liquid paraffin to fabricate a thermally conductive h-BN/chitosan composite PCM. Since paraffin was impregnated into the aerogels by capillary forces and surface tensions, the resulting form-stable composite PCMs presented exceptionally stable thermo-physical characteristics, *e.g.*, latent heat of 118.4 J g^{-1} and thermal conductivity of 1.14 W m^{-1} K^{-1}.

In the context of cost-effective energy storage systems, MoS_2 is also becoming popular for aerogel-based composite PCMs due to its abundant resources and facile extraction. Besides, MoS_2 has significant solar absorbance in the infrared region owing to its high broadband antireflective characteristics.[283] For instance, self-assembled 3D flower-like structures of MoS_2 nanosheets were reported to enhance the light-to-thermal conversion efficiency of 1-OC up to 85.5%.[284]

In an intriguing study, Gue *et al.*[285] designed a bilayer aerogel system composed of MoS_2 and montmorillonite (MMT) integrated with PCMs for efficient solar energy harvesting and freshwater desalination. This system had two parts: (1) a bottom layer of MMT aerogel for water supply and thermal insulation, and (2) an upper layer of MoS_2 and paraffin/SiO_2 aerogel-based phase change microcapsules for solar energy harvesting, storage, and steam generation (Fig. 8g–l). The composite PCMs have a latent heat of 177.85 J g^{-1}, allowing the system to store solar thermal energy during illumination and release heat for continuous seawater desalination during darkness. The results showed that the MoS_2/MMT solar evaporator realized a water evaporation rate of 1.32 kg m^{-2} h^{-1} and an evaporation efficiency of 86.22% under a light intensity of 1 kW m^{-2}. Even when there was no sunlight, the evaporation rate and efficiency were still as high as 0.71 kg m^{-2} h^{-1} and 44.36% after 20 minutes of running.

Phosphorene (PR) nanoflakes are among other 2D nanomaterials used in developing high-performance aerogel-based composite PCMs. What sets PR nanoflakes apart is their unique properties, including a tunable bandgap, high charge mobility, and excellent biocompatibility.[56,286] Their anisotropic orthorhombic structure means that they are ductile along one of the in-plane crystal directions but stiff along the other.[56,286] This property gives them unusual mechanical, electronic, optical, and transport properties that reflect the anisotropy of the lattice. PR nanoflakes also exhibit superior photothermal conversion efficiency near-infrared light, rendering them very promising for photothermal utilization. Therefore, incorporating PR nanoflakes into aerogel-based composite PCMs can enhance the mechanical performance of the hybrid aerogel through a nanoscale reinforcement effect, as well as promote external heat transfer through enhanced infrared photothermal conversion from a high-temperature target. To this end, Shi *et al.*[56] developed flexible and foldable composite films based on polyimide/PR hybrid aerogel and PCMs for infrared stealth and thermal camouflage applications. The composite films were obtained by fabricating a polyimide/PR hybrid aerogel through prepolymerization, film casting, freeze-drying, and thermal imidization, followed by vacuum impregnation of PEG as a PCM into the aerogel framework. The combination of polyimide and PR nanoflakes endows the hybrid aerogels an effective enhancement in mechanical properties, near infrared absorption, and infrared photothermal conversion. The resultant composite films not only present prominent tensile and fatigue-resistant performance but also exhibit good thermal regulation capability with a high latent-heat capacity of over 150 J g^{-1}. Moreover, the composite films demonstrate good infrared stealth

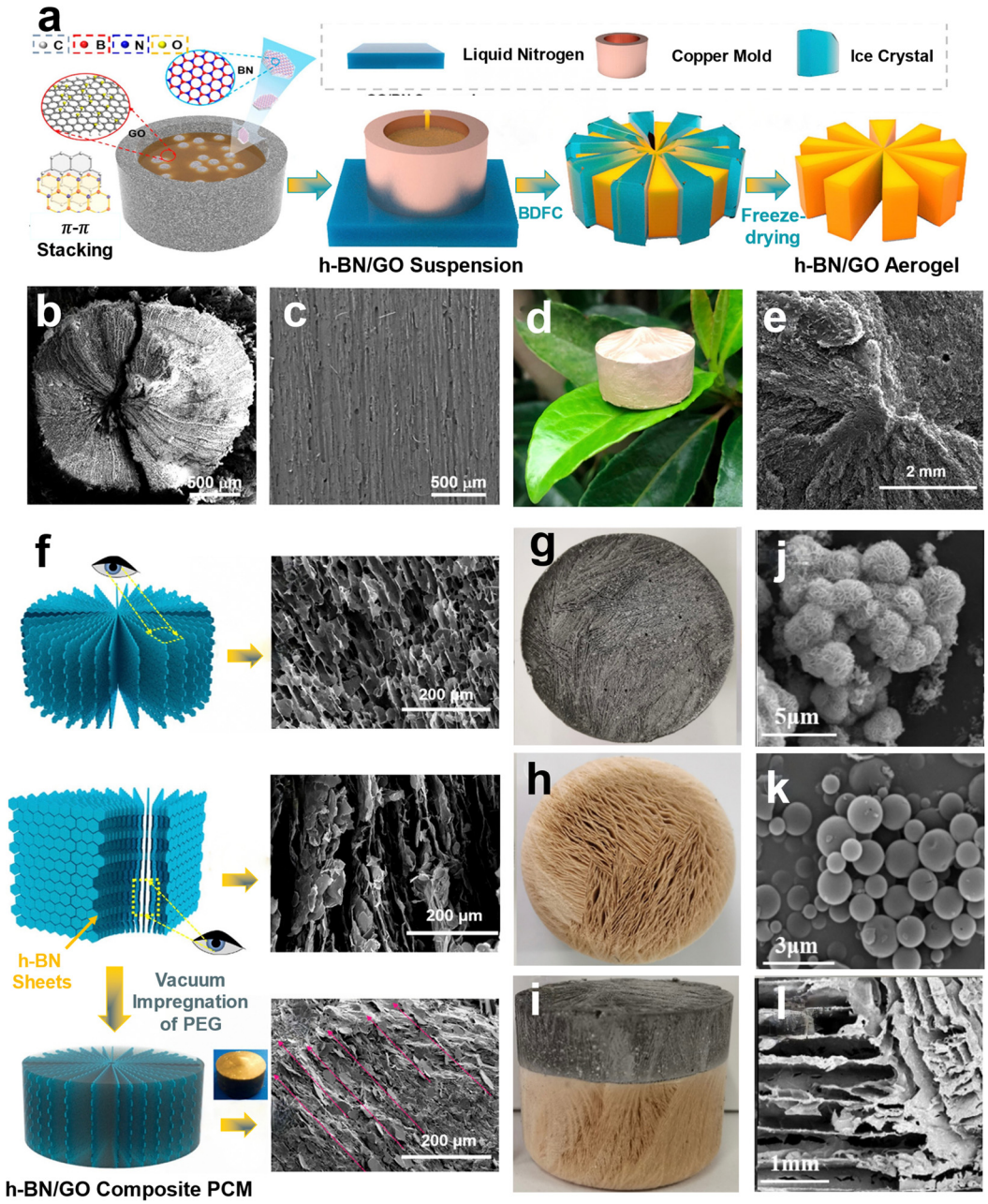

Fig. 8 (a) Schematic illustration of BDFC approach for preparing bioinspired h-BN/GO aerogel. (b) Vertically and (c) radially aligned channels of the water transportation system within towering confiner trees. (d) Optical images of h-BN/GO aerogel. (e) Cross-sectional morphology of the corresponding aerogel. (f) Schematic and SEM images of the cross-sectional and longitudinal section of the h-BN/GO scaffold before and after PCM impregnation. (a–f) Reproduced with permission.[281] Copyright 2020, American Chemical Society. (g–i) Optical images of bilayer aerogel systems. (j–l) SEM images of (j) MoS_2 and (k) paraffin/SiO_2 aerogel-based phase change microcapsules and (l) MMT aerogels. (g–l) Reproduced with permission.[285] Copyright 2022, Elsevier.

and thermal camouflage performance on high-temperature targets through effective thermal buffer and insulation.

Zheng *et al.*[287] also developed composites of PCMs and PR nanosheets for efficient solar energy capture and photothermal conversion. The composite was basically made of polyimide/PR hybrid aerogels and PEG as the PCM. The synthesis involved the fabrication of a series of hybrid aerogels by incorporating different loadings of PR nanosheets into polyimide using freeze-drying and thermal imidization techniques. The resulting hybrid aerogels were then impregnated with PEG through vacuum impregnation to create the composite PCMs. The introduction of PR nanosheets increased the volume capacity of the hybrid aerogels, leading to a remarkable improvement in the loading amount of PEG. Interestingly, the hybrid aerogels displayed a lightweight nature with a density of 21.9 mg cm^{-3} when 16 wt% of PR nanosheets were incorporated. This resulted in an extremely high PEG loading of 4067% in the aerogel system. Additionally, the incorporation of PR nanosheets into the polyimide matrix enhanced solar light absorption and photothermal energy conversion for the hybrid aerogel/PEG

composites. The resulting hybrid aerogel/PEG composites exhibited a high latent-heat capacity of over 170 J g^{-1} and a high photothermal conversion efficiency of 82.5%. Moreover, the composites demonstrated good thermal impact resistance by retaining their original shape and form even after heating at 80 °C for 20 min. Furthermore, the composite PCMs maintained high thermal cycle stability after thermal cycling 500 times.

5. Current challenges and future prospects

The future of aerogel-based composite PCMs seems to be boundless in thermal management systems, mainly due to their form stability and enhanced thermal conductivity compared to pure PCMs. These unique characteristics of composite PCMs are influenced by their supporting scaffolds. In this regard, we have reviewed various methods for aerogel fabrication, including drying approaches and pre-treatment methods, as well as advances in 2D nanomaterial-based aerogels and their potential uses in composite PCMs. Additionally, we have discussed the versatile advances proposed in 2D nanomaterial aerogel-based composite PCMs, specifically focusing on the type and functionality of the scaffolds.

Despite these advancements, large-scale fabrication of aerogels yet remains a challenge for practical applications in both industrial and domestic settings. The study presented by Yang *et al.*[174] on scalable fabrication ($\sim$1 m^2) of structure-intact graphene-based aerogels through simple freezing and air-drying of chemically reduced foam-like GO suspension has the potential to address this challenge. However, such a scalable process is yet to be explored for cost-effective aerogel-based composite PCMs. On the other hand, mechanical robustness and flexibility are among the other core challenges of aerogel-based composite PCMs. Up to now, the research on flexible and foldable composite PCMs has been limited, with only a few studies, such as Sun *et al.*[99] (flexible graphene/PVDFHFP aerogel-based composite PCMs) and Shi *et al.*[56] (flexible and foldable polyimide/PR hybrid aerogel-based composite PCMs), attempting to address the challenges in this area. As such, there is a significant need for further exploration of flexible and foldable composite PCMs, as they represent an important research topic in this field. All in all, if composite PCMs become flexible, a myriad of applications, from wearable heat sensors to thermal resistance clothing, can be added to PCM-based thermal management systems.

Expanding the range of applications for aerogel-based composite PCMs is an area that requires further research. Currently, most studies on these materials focus primarily on thermal management systems and related topics, such as solar desalination and photo-thermal energy conversion. However, the functionality of the aerogel-based scaffolds is not fully adopted in composite PCMs. The study by Zhao *et al.*,[263] which used aerogel-based composite PCMs of graphene for thermal management and heat sensing, is one of the rare examples of utilizing the functionality of aerogel-based scaffolds in the final composite PCMs. In this regard, we can also refer to the work of Shi *et al.*,[100] where a polyimide/graphene/Fe_3O_4 hybrid aerogel was used as a skeleton to produce multifunctional composite PCMs with simultaneous EMI and infrared shielding capabilities. All in all, we expect that future studies will follow a similar trend to take advantage of the inherent functionalities of aerogel skeletons and achieve multi-responsive and multifunctional composite PCMs with novel characteristics.

Last but not least, there is no in-depth comparative investigation on the phase transition enthalpy, specific heat, expansion coefficient, and energy storage capacity of various 2D aerogel-based composite PCMs. Such a perspective regarding these heat transfer mechanisms is crucial to select the best candidate for the large-scale fabrication of composite PCMs. Additionally, it is important to investigate the pros and cons of various 2D aerogel scaffolds before using them for composite PCMs. For example, MXenes showcase great excellent water processability, electrical conductivity, and thermal characteristics, which are necessary for developing multifunctional thermal management composites. However, this class of 2D nanomaterials is susceptible to oxidation and thermal degradations.[326] Therefore, it is necessary to investigate the long-term effects of these shortcomings on the overall performance of MXene-based composite PCMs to ensure their suitability for practical applications.

Conflicts of interest

There are no conflicts to declare.

Acknowledgements

The authors acknowledge the Syilx Okanagan Nation for the use of their traditional, ancestral, and unceded territory, the land on which the research was conducted. The authors acknowledge the support of the Natural Sciences and Engineering Research Council of Canada (NSERC) [funding reference number ALLRP 555586-20]. Dr Arjmand appreciate the financial support provided by the University of British Columbia (UBC), the Canada Research Chairs Program, and Zentek Ltd.

References

1 R. Gulfam, P. Zhang and Z. Meng, *Appl. Energy*, 2019, **238**, 582–611.
2 B. Zhao, R. Zhu, N. Sheng, C. Zhu and Z. Rao, *Energy Fuels*, 2022, **36**, 10354–10363.
3 X. Min, B. Sun, S. Chen, M. Fang, X. Wu, Y. G. Liu, A. Abdelkader, Z. Huang, T. Liu, K. Xi and R. Vasant Kumar, *Energy Storage Mater.*, 2019, **16**, 597–606.
4 Y. Zhao, X. Min, Z. Ding, S. Chen, C. Ai, Z. Liu, T. Yang, X. Wu, Y. G. Liu, S. Lin, Z. Huang, P. Gao, H. Wu and M. Fang, *Adv. Sci.*, 2020, **7**, 1902051.
5 D. Lencer, M. Salinga and M. Wuttig, *Adv. Mater.*, 2011, **23**, 2030–2058.
6 K. Pielichowska and K. Pielichowski, *Prog. Mater. Sci.*, 2014, **65**, 67–123.

7 M. Wuttig, H. Bhaskaran and T. Taubner, *Nat. Photonics*, 2017, **11**, 465–476.
8 Z. Zhu, P. G. Evans, R. F. Haglund, Jr. and J. G. Valentine, *Nano Lett.*, 2017, **17**, 4881–4885.
9 P. Lian, R. Yan, Z. Wu, Z. Wang, Y. Chen, L. Zhang and X. Sheng, *Adv. Compos. Hybrid Mater.*, 2023, **6**, 74.
10 J.-F. Su, X.-Y. Wang, S. Han, X.-L. Zhang, Y.-D. Guo, Y.-Y. Wang, Y.-Q. Tan, N.-X. Han and W. Li, *J. Mater. Chem. A*, 2017, **5**, 23937–23951.
11 L. Yang, X. Jin, Y. Zhang and K. Du, *J. Cleaner Prod.*, 2021, **287**, 124432.
12 E. Zdraveva, J. Fang, B. Mijovic and T. Lin, *Ind. Eng. Chem. Res.*, 2015, **54**, 8706–8712.
13 J. T. McCann, M. Marquez and Y. Xia, *Nano Lett.*, 2006, **6**, 2868–2872.
14 R. K. Sharma, P. Ganesan, V. V. Tyagi, H. S. C. Metselaar and S. C. Sandaran, *Energy Convers. Manage.*, 2015, **95**, 193–228.
15 Y. Yuan, N. Zhang, W. Tao, X. Cao and Y. He, *Renewable Sustainable Energy Rev.*, 2014, **29**, 482–498.
16 A. Fallahi, G. Guldentops, M. Tao, S. Granados-Focil and S. Van Dessel, *Appl. Therm. Eng.*, 2017, **127**, 1427–1441.
17 H. Ke, *Sol. Energy*, 2018, **173**, 1197–1206.
18 Y. Ueki, H. Murashima and M. Shibahara, *Int. J. Heat Mass Transfer*, 2020, **163**, 120463.
19 R. Shen, L. Liu, Y. Cao, L. Zhang, X. Sheng and Y. Chen, *Sol. Energy*, 2022, **242**, 287–297.
20 C. Liu, F. Li, L. P. Ma and H. M. Cheng, *Adv. Mater.*, 2010, **22**, E28–62.
21 M. Graham, J. A. Coca-Clemente, E. Shchukina and D. Shchukin, *J. Mater. Chem. A*, 2017, **5**, 13683–13691.
22 K. Kant, A. Shukla and A. Sharma, *Sol. Energy Mater.*, 2017, **172**, 82–92.
23 X. Chen, P. Cheng, Z. Tang, X. Xu, H. Gao and G. Wang, *Adv. Sci.*, 2021, **8**, 2001274.
24 C. Amaral, R. Vicente, P. A. A. P. Marques and A. Barros-Timmons, *Renewable Sustainable Energy Rev.*, 2017, **79**, 1212–1228.
25 M. M. Joybari, F. Haghighat and S. Seddegh, *Sol. Energy*, 2017, **158**, 711–720.
26 S. A. Mohamed, F. A. Al-Sulaiman, N. I. Ibrahim, M. H. Zahir, A. Al-Ahmed, R. Saidur, B. S. Yılbaş and A. Z. Sahin, *Renewable Sustainable Energy Rev.*, 2017, **70**, 1072–1089.
27 A. Chibani, S. Merouani, F. Benmoussa, M. H. Abdellattif, A. Erto, B.-H. Jeon and Y. Benguerba, *J. Environ. Chem. Eng.*, 2021, **9**, 106744.
28 Y. Lin, Y. Jia, G. Alva and G. Fang, *Renewable Sustainable Energy Rev.*, 2018, **82**, 2730–2742.
29 P. Manoj Kumar, D. Sudarvizhi, P. M. J. Stalin, A. Aarif, R. Abhinandhana, A. Renuprasanth, V. Sathya and N. T. Ezhilan, *Mater. Today: Proc*, 2021, **45**, 7876–7880.
30 M. A. Sheik, M. K. Aravindan, N. Beemkumar, P. K. Chaurasiya and J. A. Dhanraj, *Arabian J. Sci. Eng.*, 2022, **47**, 15899–15913.
31 S. Song, F. Qiu, W. Zhu, Y. Guo, Y. Zhang, Y. Ju, R. Feng, Y. Liu, Z. Chen, J. Zhou, C. Xiong and L. Dong, *Sol. Energy Mater.*, 2019, **193**, 237–245.
32 J. Chen, Z. Mo, Y. Chen, P. Mo, Z. Hu, X. Chen, J. Yu, Z. Hao, X. Zeng, R. Sun and J. Xu, *ACS Appl. Energy Mater.*, 2022, **5**, 11669–11683.
33 S. Chen, A. L. Moore, W. Cai, J. W. Suk, J. An, C. Mishra, C. Amos, C. W. Magnuson, J. Kang, L. Shi and R. S. Ruoff, *ACS Nano*, 2011, **5**, 321–328.
34 M. Li and B. Mu, *Appl. Energy*, 2019, **242**, 695–715.
35 Y. He, H. Li, F. Luo, Y. Jin, B. Huang and Q. Qian, *Composites, Part A*, 2021, **151**, 106638.
36 H. Liu, Z. Han, Q. Wang, X. Wang, D. Wu and X. Wang, *Appl. Surf. Sci.*, 2021, **562**, 150211.
37 Z. Sun, H. Liu and X. Wang, *Composites, Part B*, 2022, **242**, 110112.
38 H. Liu, X. Tian, M. Ouyang, X. Wang, D. Wu and X. Wang, *Renewable Energy*, 2021, **179**, 47–64.
39 H. Liu, X. Wang and D. Wu, *Sustainable Energy Fuels*, 2019, **3**, 1091–1149.
40 M. Graham, E. Shchukina, P. F. De Castro and D. Shchukin, *J. Mater. Chem. A*, 2016, **4**, 16906–16912.
41 Y. Konuklu, H. O. Paksoy and M. Unal, *Appl. Energy*, 2015, **150**, 335–340.
42 A. Sarı, C. Alkan and C. Bilgin, *Appl. Energy*, 2014, **136**, 217–227.
43 A. Sarı, C. Alkan, D. Kahraman Döğüşcü and A. Biçer, *Sol. Energy Mater.*, 2014, **126**, 42–50.
44 P. Singh, R. K. Sharma, M. Khalid, R. Goyal, A. Sarı and V. V. Tyagi, *Sol. Energy Mater.*, 2022, **246**, 111896.
45 D. G. Atinafu, B. Y. Yun, S. Yang, H. Yuk, S. Wi and S. Kim, *Energy Storage Mater.*, 2021, **42**, 164–184.
46 R. Ye, H. Jiang, J. Wang, X. Yang and X. Shu, *Sol. Energy Mater.*, 2022, **238**, 111584.
47 H. Liu, Z. Zheng, Z. Qian, Q. Wang, D. Wu and X. Wang, *Sol. Energy Mater.*, 2021, **229**, 111140.
48 R. Chatterjee, D. Beysens and S. Anand, *Adv. Mater.*, 2019, **31**, e1807812.
49 A. L. Cottrill, A. T. Liu, Y. Kunai, V. B. Koman, A. Kaplan, S. G. Mahajan, P. Liu, A. R. Toland and M. S. Strano, *Nat. Commun.*, 2018, **9**, 664.
50 C. Liu, J. Zhang, J. Liu, Z. Tan, Y. Cao, X. Li and Z. Rao, *Angew. Chem., Int. Ed.*, 2021, **60**, 13978–13987.
51 S. Zhang, Q. Li, N. Yang, Y. Shi, W. Ge, W. Wang, W. Huang, X. Song and X. Dong, *Adv. Funct. Mater.*, 2019, **29**, 1906805.
52 X. Chen, H. Gao, Z. Tang and G. Wang, *Cell Rep. Phys. Sci.*, 2020, **1**, 100218.
53 Y. Cai, Q. Wei, F. Huang, S. Lin, F. Chen and W. Gao, *Renew. Energy*, 2009, **34**, 2117–2123.
54 E. Pakdel, M. Naebe, L. Sun and X. Wang, *ACS Appl. Mater. Interfaces*, 2019, **11**, 13039–13057.
55 J. Shi, M. Qin, W. Aftab and R. Zou, *Energy Storage Mater.*, 2021, **41**, 321–342.
56 T. Shi, Z. Zheng, H. Liu, D. Wu and X. Wang, *Compos. Sci. Technol.*, 2022, **217**, 109127.
57 Z. Tao, X. Chen, M. Yang, X. Xu, Y. Sun, Y. Li, J. Wang and G. Wang, *Sol. Energy Mater.*, 2020, **215**, 110600.
58 H. Fang, J. Lin, L. Zhang, A. Chen, F. Wu, L. Geng and X. Peng, *Carbohydr. Polym.*, 2020, **249**, 116836.

59 X. Liu and Z. Rao, *J. Energy Storage*, 2020, **32**, 101860.
60 R. Shen, M. Weng, L. Zhang, J. Huang and X. Sheng, *Composites, Part A*, 2022, **163**, 107248.
61 P. Min, J. Liu, X. Li, F. An, P. Liu, Y. Shen, N. Koratkar and Z.-Z. Yu, *Adv. Funct. Mater.*, 2018, **28**, 1805365.
62 J. Yang, X. Li, S. Han, R. Yang, P. Min and Z.-Z. Yu, *J. Mater. Chem. A*, 2018, **6**, 5880–5886.
63 S. Wang, K. Lei, Z. Wang, H. Wang and D. Zou, *Chem. Eng. J.*, 2022, **438**, 135559.
64 M. Yadav, N. Pasarkar, A. Naikwadi and P. Mahanwar, *Polym. Bull.*, 2022, 1–31.
65 D. He and M. H. M. Isa, *Adv. Civ. Eng. Mater.*, 2023, **310**, DOI: 10.1007/978-981-19-8024-4_20.
66 M. Pomianowski, P. Heiselberg and Y. Zhang, *Energy Build.*, 2013, **67**, 56–69.
67 L. F. Cabeza, A. Castell, C. D. Barreneche, A. De Gracia and A. Fernández, *Renewable Sustainable Energy Rev.*, 2011, **15**, 1675–1695.
68 P. K. Kushwaha, N. K. Sharma, A. Kumar and C. S. Meena, *Buildings*, 2023, **13**, 79.
69 S. Chandel and T. Agarwal, *Renewable Sustainable Energy Rev.*, 2017, **67**, 581–596.
70 R. Sharma, P. Ganesan, V. Tyagi, H. Metselaar and S. Sandaran, *Energy Convers. Manage.*, 2015, **95**, 193–228.
71 X. Chen, P. Cheng, Z. Tang, X. Xu, H. Gao and G. Wang, *Adv. Sci.*, 2021, **8**, 2001274.
72 Y. Tao, C. Lin and Y. He, *Energy Convers. Manage.*, 2015, **97**, 103–110.
73 C. Li, Q. Li and Y. Ding, *Appl. Energy*, 2019, **247**, 374–388.
74 A. C. Evers, M. A. Medina and Y. Fang, *Build. Environ.*, 2010, **45**, 1762–1768.
75 A. Sangeetha, S. Shanmugan, A. J. Alrubaie, M. M. Jaber, H. Panchal, M. E. H. Attia, A. H. Elsheikh, D. Mevada and F. A. Essa, *Desalination*, 2023, **551**, 116367.
76 S. Rostami, M. Afrand, A. Shahsavar, M. Sheikholeslami, R. Kalbasi, S. Aghakhani, M. S. Shadloo and H. F. Oztop, *Energy*, 2020, **211**, 118698.
77 F. Javadi, H. Metselaar and P. Ganesan, *Sol. Energy*, 2020, **206**, 330–352.
78 R. Raud, R. Jacob, F. Bruno, G. Will and T. A. Steinberg, *Renewable Sustainable Energy Rev.*, 2017, **70**, 936–944.
79 E. Van Artsdalen and I. Yaffe, *J. Phys. Chem.*, 1955, **59**, 118–127.
80 R. DiGuilio and A. S. Teja, *Int. J. Thermophys.*, 1992, **13**, 855–871.
81 R. Parameshwaran, K. Deepak, R. Saravanan and S. Kalaiselvam, *Appl. Energy*, 2014, **115**, 320–330.
82 A. Pasupathy, R. Velraj and R. Seeniraj, *Renewable Sustainable Energy Rev.*, 2008, **12**, 39–64.
83 M.-H. Sun, S.-Z. Huang, L.-H. Chen, Y. Li, X.-Y. Yang, Z.-Y. Yuan and B.-L. Su, *Chem. Soc. Rev.*, 2016, **45**, 3479–3563.
84 M. M. Umair, Y. Zhang, K. Iqbal, S. Zhang and B. Tang, *Appl. Energy*, 2019, **235**, 846–873.
85 M. Wu, S. Wu, Y. Cai, R. Wang and T. Li, *Energy Storage Mater.*, 2021, **42**, 380–417.
86 Y. Konuklu, H. O. Paksoy and M. Unal, *Appl. Energy*, 2015, **150**, 335–340.
87 A. Sarı, C. Alkan and C. Bilgin, *Appl. Energy*, 2014, **136**, 217–227.
88 A. Sarı, C. Alkan, D. K. Döğüşcü and A. Biçer, *Solar Energy Mater. Solar Cells*, 2014, **126**, 42–50.
89 P. Liu, X. Chen, Y. Li, P. Cheng, Z. Tang, J. Lv, W. Aftab and G. Wang, *ACS Nano*, 2022, **16**, 15586–15626.
90 J. Zhang, S. Wang, S. Zhang, Q. Tao, L. Pan, Z. Wang, Z. Zhang, Y. Lei, S. Yang and H. Zhao, *J. Phys. Chem. C*, 2011, **115**, 20061–20066.
91 Y. Zhu, S. Liang, K. Chen, X. Gao, P. Chang, C. Tian, J. Wang and Y. Huang, *Energy Convers. Manage.*, 2015, **105**, 908–917.
92 S. Zhang, S. Wang, J. Zhang, Y. Jiang, Q. Ji, Z. Zhang and Z. Wang, *J. Phys. Chem. C*, 2013, **117**, 23412–23417.
93 L. Pan, Q. Tao, S. Zhang, S. Wang, J. Zhang, S. Wang, Z. Wang and Z. Zhang, *Sol. Energy Mater.*, 2012, **98**, 66–70.
94 H. Luo, Y. Huang, D. Wang and J. Shi, *J. Polym. Sci., Part B: Polym. Phys.*, 2013, **51**, 376–383.
95 S. Sinha-Ray, R. Sahu and A. Yarin, *Soft Matter*, 2011, **7**, 8823–8827.
96 C. Nie, X. Tong, S. Wu, S. Gong and D. Peng, *RSC Adv.*, 2015, **5**, 92812–92817.
97 S. Zhang, Q. Tao, Z. Wang and Z. Zhang, *J. Mater. Chem.*, 2012, **22**, 20166–20169.
98 B. Yang, T. Zhang, J. Wang, J. Lv, Y. Zheng, Y. Zhang and Y. Wang, *Sol. Energy Mater.*, 2022, **247**, 111948.
99 K. Sun, H. Dong, Y. Kou, H. Yang, H. Liu, Y. Li and Q. Shi, *Chem. Eng. J.*, 2021, **419**, 129637.
100 T. Shi, Z. Zheng, H. Liu, D. Wu and X. Wang, *Nanomaterials*, 2021, **11**, 3038.
101 Y. Cao, Z. Zeng, D. Huang, Y. Chen, L. Zhang and X. Sheng, *Nano Res.*, 2022, **15**, 8524–8535.
102 S. S. Kistler, *Nature*, 1931, **127**, 741.
103 J. P. Vareda, A. Lamy-Mendes and L. Durães, *Microporous Mesoporous Mater.*, 2018, **258**, 211–216.
104 M. A. Aegerter, N. Leventis and M. Koebel, *Aerogels Handbook*, Springer, New York, NY, USA, 2011.
105 B. Liu, J. Zhuang and G. Wei, *Environ. Sci.: Nano*, 2020, **7**, 2195–2213.
106 D. Zhu, B. Liu and G. Wei, *Biosensors*, 2021, **11**, 259.
107 P. Gupta, B. Singh, A. K. Agrawal and P. K. Maji, *Mater. Des.*, 2018, **158**, 224–236.
108 H. Kong, Y. Chen, G. Yang, B. Liu, L. Guo, Y. Wang, X. Zhou and G. Wei, *Nanoscale Horiz.*, 2022, **7**, 112–140.
109 D. M. Smith, A. Maskara and U. Boes, *J. Non-Cryst. Solids*, 1998, **225**, 254–259.
110 A. A. Balandin, *Nat. Mater.*, 2011, **10**, 569–581.
111 D. L. Nika and A. A. Balandin, *J. Phys. Condens.*, 2012, **24**, 233203.
112 K. S. Novoselov, A. K. Geim, S. V. Morozov, D.-E. Jiang, Y. Zhang, S. V. Dubonos, I. V. Grigorieva and A. A. Firsov, *Science*, 2004, **306**, 666–669.
113 D. Golberg, Y. Bando, Y. Huang, T. Terao, M. Mitome, C. Tang and C. Zhi, *ACS Nano*, 2010, **4**, 2979–2993.
114 B. Radisavljevic, A. Radenovic, J. Brivio, V. Giacometti and A. Kis, *Nat. Nanotechnol.*, 2011, **6**, 147–150.

115 X. Zhang, R. Lv, A. Wang, W. Guo, X. Liu and J. Luo, *Angew. Chem.*, 2018, **130**, 15248–15253.
116 Y.-M. Lin, C. Dimitrakopoulos, K. A. Jenkins, D. B. Farmer, H.-Y. Chiu, A. Grill and P. Avouris, *Science*, 2010, **327**, 662.
117 T. Mueller, F. Xia and P. Avouris, *Nat. Photonics*, 2010, **4**, 297–301.
118 A. Pospischil, M. M. Furchi and T. Mueller, *Nat. Nanotechnol.*, 2014, **9**, 257–261.
119 X. Yang, C. Cheng, Y. Wang, L. Qiu and D. Li, *Science*, 2013, **341**, 534–537.
120 Y. Li, H. Wang, L. Xie, Y. Liang, G. Hong and H. Dai, *J. Am. Chem. Soc.*, 2011, **133**, 7296–7299.
121 B. Liu, L. Chen, G. Liu, A. N. Abbas, M. Fathi and C. Zhou, *ACS Nano*, 2014, **8**, 5304–5314.
122 K. Raagulan, B. M. Kim and K. Y. Chai, *Nanomaterials*, 2020, **10**, 702.
123 M. Kamkar, A. Ghaffarkhah, R. Ajdary, Y. Lu, F. Ahmadijokani, S. E. Mhatre, E. Erfanian, U. Sundararaj, M. Arjmand and O. J. Rojas, *Small*, 2022, 2200220.
124 S. A. Hashemi, A. Ghaffarkhah, E. Hosseini, S. Bahrani, P. Najmi, N. Omidifar, S. M. Mousavi, M. Amini, M. Ghaedi and S. Ramakrishna, *Matter*, 2022, **5**, 3807–3868.
125 N. Howe and S. Bundell, *Nature*, 2020, DOI: **10.1038/d41586-020-02448-5**.
126 R.-L. Liu, W.-J. Ji, T. He, Z.-Q. Zhang, J. Zhang and F.-Q. Dang, *Carbon*, 2014, **76**, 84–95.
127 X. Fu, J.-Y. Choi, P. Zamani, G. Jiang, M. A. Hoque, F. M. Hassan and Z. Chen, *ACS Appl. Mater. Interfaces*, 2016, **8**, 6488–6495.
128 X. Huang, X. Chen, A. Li, D. Atinafu, H. Gao, W. Dong and G. Wang, *Chem. Eng. J.*, 2019, **356**, 641–661.
129 Y. Li, X. Huang, G. Hai, J. Lv, Z. Tao and G. Wang, *Chem. Eng. J.*, 2022, **428**, 131075.
130 M. E. El-Naggar, S. I. Othman, A. A. Allam and O. M. Morsy, *Int. J. Biol. Macromol.*, 2020, **145**, 1115–1128.
131 C. Simón-Herrero, S. Caminero-Huertas, A. Romero, J. L. Valverde and L. Sánchez-Silva, *J. Mater. Sci.*, 2016, **51**, 8977–8985.
132 A. Mirtaghavi, J. Luo and R. Muthuraj, *J. Compos. Sci.*, 2020, **4**(4), 152.
133 J. Yan, T. Wu, Z. Ding and X. Li, *Carbohydr. Polym.*, 2016, **136**, 1288–1296.
134 G. M. Vladimirovich and V. P. Melnikov, *Graphene Oxide-Applications and Opportunities*, 2018, 39–55.
135 M. Kotal, J. Kim, J. Oh and I.-K. Oh, *Front. Mater.*, 2016, **3**, 29.
136 M. Berrio, A. Oñate, A. Salas, K. Fernández and M. Meléndrez, *Mater. Today Chem.*, 2021, **20**, 100422.
137 G. Nassar, E. Daou, R. Najjar, M. Bassil and R. Habchi, *Carbon Trends*, 2021, **4**, 100065.
138 R. Castaldo, R. Avolio, M. Cocca, M. E. Errico, M. Lavorgna, J. Šalplachta, C. Santillo and G. Gentile, *Chem. Eng. J.*, 2022, **430**, 133162.
139 Y. M. Shul'ga, E. Kabachkov, S. Baskakov and Y. V. Baskakova, *Russ. J. Phys. Chem.*, 2019, **93**, 296–300.
140 W. Chen, L. Yan and P. Bangal, *J. Phys. Chem. C*, 2010, **114**, 19885–19890.
141 S. P. Lee, G. A. Ali, H. Hegazy, H. N. Lim and K. F. Chong, *Energy Fuels*, 2021, **35**, 4559–4569.
142 K. Ghosh, C. Y. Yue, M. M. Sk, R. K. Jena and S. Bi, *Sustain. Energy Fuels*, 2018, **2**, 280–293.
143 M. Serrapede, M. Fontana, A. Gigot, M. Armandi, G. Biasotto, E. Tresso and P. Rivolo, *Materials*, 2020, **13**, 594.
144 T. Shen, Z. Zhao, Q. Zhong, Y. Qin, P. Zhang and Z.-X. Guo, *RSC Adv.*, 2019, **9**, 13042–13047.
145 Q. Zhang, W. Lu, M. Wu, G. Qi, Y. Yuan, J. Li, H. Su and H. Zhang, *J. Environ. Manage.*, 2022, **302**, 114044.
146 X. Wei, T. Huang, J.-H. Yang, N. Zhang, Y. Wang and Z.-W. Zhou, *J. Hazard. Mater.*, 2017, **335**, 28–38.
147 H. Ji, J. Li, J. Zhang and Y. Yan, *Composites, Part A*, 2019, **123**, 158–169.
148 Z. Zhao, X. Wang, J. Qiu, J. Lin, D. Xu, C. A. Zhang, M. Lv and X. Yang, *Rev. Adv. Mater. Sci.*, 2014, **36**, 137–151.
149 L. Jiang, Y. Wen, Z. Zhu, X. Liu and W. Shao, *Chemosphere*, 2021, **265**, 129169.
150 B. Anasori, M. R. Lukatskaya and Y. Gogotsi, *Nat. Rev. Mater.*, 2017, **2**, 1–17.
151 S. Shi, B. Qian, X. Wu, H. Sun, H. Wang, H. B. Zhang, Z. Z. Yu and T. P. Russell, *Angew. Chem., Int. Ed.*, 2019, **58**, 18171–18176.
152 X. Liu, Z. Lu, X. Huang, J. Bai, C. Li, C. Tu and X. Chen, *J. Power Sources*, 2021, **516**, 230682.
153 T. Chen, J. Wang, X. Wu, Z. Li and S. Yang, *Appl. Surf. Sci.*, 2021, **566**, 150719.
154 T. Shang, Z. Lin, C. Qi, X. Liu, P. Li, Y. Tao, Z. Wu, D. Li, P. Simon and Q. H. Yang, *Adv. Funct. Mater.*, 2019, **29**, 1903960.
155 Y.-Z. Zhang, J. K. El-Demellawi, Q. Jiang, G. Ge, H. Liang, K. Lee, X. Dong and H. N. Alshareef, *Chem. Soc. Rev.*, 2020, **49**, 7229–7251.
156 X. Zhou, J. Wen, X. Ma and H. Wu, *J. Colloid Interface Sci.*, 2022, **624**, 505–514.
157 Y. Deng, T. Shang, Z. Wu, Y. Tao, C. Luo, J. Liang, D. Han, R. Lyu, C. Qi and W. Lv, *Adv. Mater.*, 2019, **31**, 1902432.
158 T. Fukasawa, M. Ando, T. Ohji and S. Kanzaki, *J. Am. Ceram. Soc.*, 2001, **84**, 230–232.
159 G. Shao, D. A. H. Hanaor, X. Shen and A. Gurlo, *Adv. Mater.*, 2020, **32**, e1907176.
160 W. Liao, H.-B. Zhao, Z. Liu, S. Xu and Y.-Z. Wang, *Composites, Part B*, 2019, **173**, 107036.
161 B. Wicklein, A. Kocjan, G. Salazar-Alvarez, F. Carosio, G. Camino, M. Antonietti and L. Bergstrom, *Nat. Nanotechnol.*, 2015, **10**, 277–283.
162 M. Li, X. Dai, W. Gao and H. Bai, *Acc. Mater. Res.*, 2022, **3**, 1173–1185.
163 C. Wang, X. Chen, B. Wang, M. Huang, B. Wang, Y. Jiang and R. S. Ruoff, *ACS Nano*, 2018, **12**, 5816–5825.
164 P. Pieranski, *Phys. Rev. Lett.*, 1980, **45**, 569.
165 B. P. Binks, *Curr. Opin. Colloid Interface Sci.*, 2002, **7**, 21–41.
166 M. Kamkar, E. Erfanian, P. Bazazi, A. Ghaffarkhah, F. Sharif, G. Xie, A. Kannan, M. Arjmand, S. H. Hejazi and T. P. Russell, *Adv. Mater. Interfaces*, 2021, 2101659.
167 C. Huang, J. Forth, W. Wang, K. Hong, G. S. Smith, B. A. Helms and T. P. Russell, *Nat. Nanotechnol.*, 2017, **12**, 1060–1063.

168 J. Forth, X. Liu, J. Hasnain, A. Toor, K. Miszta, S. Shi, P. L. Geissler, T. Emrick, B. A. Helms and T. P. Russell, *Adv. Mater.*, 2018, **30**, 1707603.
169 A. Toor, S. Lamb, B. A. Helms and T. P. Russell, *ACS Nano*, 2018, **12**, 2365–2372.
170 M. Kamkar, A. Ghaffarkhah, R. Ajdary, Y. Lu, F. Ahmadijokani, S. E. Mhatre, E. Erfanian, U. Sundararaj, M. Arjmand and O. J. Rojas, *Small*, 2022, **18**, e2200220.
171 D. Smith, G. Scherer and J. Anderson, *J. Non-Cryst. Solids*, 1995, **188**, 191–206.
172 J. L. Gurav, I.-K. Jung, H.-H. Park, E. S. Kang and D. Y. Nadargi, *J. Nanomater.*, 2010, **2010**, 1–11.
173 Y. Cheng, S. Zhou, P. Hu, G. Zhao, Y. Li, X. Zhang and W. Han, *Sci. Rep.*, 2017, **7**, 1439.
174 H. Yang, Z. Li, B. Lu, J. Gao, X. Jin, G. Sun, G. Zhang, P. Zhang and L. Qu, *ACS Nano*, 2018, **12**, 11407–11416.
175 H. Hu, Z. Zhao, W. Wan, Y. Gogotsi and J. Qiu, *Adv. Mater.*, 2013, **25**, 2219–2223.
176 W. Zhang, Q. Q. Kong, Z. Tao, J. Wei, L. Xie, X. Cui and C. M. Chen, *Adv. Mater. Interfaces*, 2019, **6**, 1900147.
177 L. Li, M. Zhang, X. Zhang and Z. Zhang, *J. Power Sources*, 2017, **364**, 234–241.
178 Z. Yu, M. McInnis, J. Calderon, S. Seal, L. Zhai and J. Thomas, *Nano Energy*, 2015, **11**, 611–620.
179 Y. Jiang, S. Chowdhury and R. Balasubramanian, *J. Colloid Interface Sci.*, 2019, **534**, 574–585.
180 Y. Li, F. Meng, Y. Mei, H. Wang, Y. Guo, Y. Wang, F. Peng, F. Huang and Z. Zhou, *Chem. Eng. J.*, 2020, **391**, 123512.
181 Y. Yue, N. Liu, Y. Ma, S. Wang, W. Liu, C. Luo, H. Zhang, F. Cheng, J. Rao and X. Hu, *ACS Nano*, 2018, **12**, 4224–4232.
182 H. Bai, C. Li, X. Wang and G. Shi, *Chem. Commun.*, 2010, **46**, 2376–2378.
183 L. Liu, G. Kong, Y. Zhu and C. Che, *Colloids Interface Sci. Commun.*, 2021, **45**, 100518.
184 Z. Zhou, J. Liu, X. Zhang, D. Tian, Z. Zhan and C. Lu, *Adv. Mater. Interfaces*, 2019, **6**, 1802040.
185 X. Ming, A. Guo, Q. Zhang, Z. Guo, F. Yu, B. Hou, Y. Wang, K. P. Homewood and X. Wang, *Carbon*, 2020, **167**, 285–295.
186 X. P. Li, X. Li, H. Li, Y. Zhao, W. Li, S. Yan and Z. Z. Yu, *Adv. Sustainable Syst.*, 2021, **5**, 2100263.
187 M. Ding, S. Li, L. Guo, L. Jing, S. P. Gao, H. Yang, J. M. Little, T. U. Dissanayake, K. Li, J. Yang, Y. X. Guo, H. Y. Yang, T. J. Woehl and P. Y. Chen, *Adv. Energy Mater.*, 2021, **11**(35), 2101494.
188 Z. Wang, R. Wei, J. Gu, H. Liu, C. Liu, C. Luo, J. Kong, Q. Shao, N. Wang and Z. Guo, *Carbon*, 2018, **139**, 1126–1135.
189 Y. Dai, X. Wu, Z. Liu, H.-B. Zhang and Z.-Z. Yu, *Composites, Part B*, 2020, **200**, 108263.
190 A. M. Kaczmarek and R. Van Deun, *Chem. Soc. Rev.*, 2013, **42**, 8835–8848.
191 J. Hwang, A. Ejsmont, R. Freund, J. Goscianska, B. V. Schmidt and S. Wuttke, *Chem. Soc. Rev.*, 2020, **49**, 3348–3422.
192 X. Liu, T. Ma, N. Pinna and J. Zhang, *Adv. Funct. Mater.*, 2017, **27**, 1702168.
193 X. Zhao, W. Yao, W. Gao, H. Chen and C. Gao, *Adv. Mater.*, 2017, **29**, 1701482.
194 M. B. Coskun, L. Qiu, M. S. Arefin, A. Neild, M. Yuce, D. Li and T. Alan, *ACS Appl. Mater. Interfaces*, 2017, **9**, 11345–11349.
195 L. Sheng, Y. Liang, L. Jiang, Q. Wang, T. Wei, L. Qu and Z. Fan, *Adv. Funct. Mater.*, 2015, **25**, 6545–6551.
196 R. R. Nair, P. Blake, A. N. Grigorenko, K. S. Novoselov, T. J. Booth, T. Stauber, N. M. Peres and A. K. Geim, *Science*, 2008, **320**, 1308.
197 A. K. Geim and K. S. Novoselov, *Nat. Mater.*, 2007, **6**, 183–191.
198 A. A. Balandin, S. Ghosh, W. Bao, I. Calizo, D. Teweldebrhan, F. Miao and C. N. Lau, *Nano Lett.*, 2008, **8**, 902–907.
199 L. Xu, G. Xiao, C. Chen, R. Li, Y. Mai, G. Sun and D. Yan, *J. Mater. Chem. A*, 2015, **3**, 7498–7504.
200 Z. Sui, X. Zhang, Y. Lei and Y. Luo, *Carbon*, 2011, **49**, 4314–4321.
201 H. Chang, J. Qin, P. Xiao, Y. Yang, T. Zhang, Y. Ma, Y. Huang and Y. Chen, *Adv. Mater.*, 2016, **28**, 3504–3509.
202 H. Hu, Z. Zhao, W. Wan, Y. Gogotsi and J. Qiu, *Adv. Mater.*, 2013, **25**, 2219–2223.
203 L. Liu, M. Qing, Y. Wang and S. Chen, *J. Mater. Sci. Technol.*, 2015, **31**, 599–606.
204 F. Kim, L. J. Cote and J. Huang, *Adv. Mater.*, 2010, **22**, 1954–1958.
205 B. Wicklein, A. Kocjan, G. Salazar-Alvarez, F. Carosio, G. Camino, M. Antonietti and L. Bergström, *Nat. Nanotechnol.*, 2015, **10**, 277–283.
206 Z.-Z. Pan, H. Nishihara, S. Iwamura, T. Sekiguchi, A. Sato, A. Isogai, F. Kang, T. Kyotani and Q.-H. Yang, *ACS Nano*, 2016, **10**, 10689–10697.
207 G. Zu, K. Kanamori, K. Nakanishi, X. Lu, K. Yu, J. Huang and H. Sugimura, *ACS Appl. Mater. Interfaces*, 2019, **11**, 43533–43542.
208 K. Chen, X. Tang, B. Jia, C. Chao, Y. Wei, J. Hou, L. Dong, X. Deng, T.-H. Xiao, K. Goda and L. Guo, *Nat. Mater.*, 2022, **21**, 1121–1129.
209 Z. Ouyang, C. Wang, D. Xu, H.-Y. Yu, Y. Zhou, M. Mu, D. Ge, Z. Miao and K. C. Tam, *Macromol. Mater. Eng.*, 2022, **307**, 2100834.
210 M. Yang, N. Zhao, Y. Cui, W. Gao, Q. Zhao, C. Gao, H. Bai and T. Xie, *ACS Nano*, 2017, **11**, 6817–6824.
211 J. E. Kim, T. H. Han, S. H. Lee, J. Y. Kim, C. W. Ahn, J. M. Yun and S. O. Kim, *Angew. Chem.*, 2011, **123**, 3099–3103.
212 Z. Xu and C. Gao, *ACS Nano*, 2011, **5**, 2908–2915.
213 Z. Xu and C. Gao, *Nat. Commun.*, 2011, **2**, 1–9.
214 Z. Liu, Z. Li, Z. Xu, Z. Xia, X. Hu, L. Kou, L. Peng, Y. Wei and C. Gao, *Chem. Mater.*, 2014, **26**, 6786–6795.
215 Z. Xu and C. Gao, *Acc. Chem. Res.*, 2014, **47**, 1267–1276.
216 Y. Li, W. Wei, Y. Wang, N. Kadhim, Y. Mei and Z. Zhou, *J. Mater. Chem. C*, 2019, **7**, 11783–11789.
217 N. Graeber, *Imperial College London*, 2013.
218 M. Naguib, M. Kurtoglu, V. Presser, J. Lu, J. Niu, M. Heon, L. Hultman, Y. Gogotsi and M. W. Barsoum, *Adv. Mater.*, 2011, **23**, 4248–4253.
219 B. Anasori and Û. G. Gogotsi, *2D metal carbides and nitrides (MXenes)*, Springer, 2019.
220 N. C. Frey, J. Wang, G. I. N. Vega Bellido, B. Anasori, Y. Gogotsi and V. B. Shenoy, *ACS Nano*, 2019, **13**, 3031–3041.
221 M. Naguib, O. Mashtalir, J. Carle, V. Presser, J. Lu, L. Hultman, Y. Gogotsi and M. W. Barsoum, *ACS Nano*, 2012, **6**, 1322–1331.

222 M. Naguib, V. N. Mochalin, M. W. Barsoum and Y. Gogotsi, *Adv. Mater.*, 2014, **26**, 992–1005.
223 M. Sokol, V. Natu, S. Kota and M. W. Barsoum, *Trends Chem.*, 2019, **1**, 210–223.
224 G. Deysher, C. E. Shuck, K. Hantanasirisakul, N. C. Frey, A. C. Foucher, K. Maleski, A. Sarycheva, V. B. Shenoy, E. A. Stach and B. Anasori, *ACS Nano*, 2019, **14**, 204–217.
225 A. Ghaffarkhah, M. Kamkar, Z. A. Dijvejin, H. Riazi, S. Ghaderi, K. Golovin, M. Soroush and M. Arjmand, *Carbon*, 2022, **191**, 277–289.
226 R. Bian, G. He, W. Zhi, S. Xiang, T. Wang and D. Cai, *J. Mater. Chem. C*, 2019, **7**, 474–478.
227 L. Liang, Q. Li, X. Yan, Y. Feng, Y. Wang, H.-B. Zhang, X. Zhou, C. Liu, C. Shen and X. Xie, *ACS Nano*, 2021, **15**, 6622–6632.
228 S. Zhao, H.-B. Zhang, J.-Q. Luo, Q.-W. Wang, B. Xu, S. Hong and Z.-Z. Yu, *ACS Nano*, 2018, **12**, 11193–11202.
229 M. Yang, Y. Yuan, Y. Li, X. Sun, S. Wang, L. Liang, Y. Ning, J. Li, W. Yin and Y. Li, *ACS Appl. Mater. Interfaces*, 2020, **12**, 33128–33138.
230 M. Ding, S. Li, L. Guo, L. Jing, S. P. Gao, H. Yang, J. M. Little, T. U. Dissanayake, K. Li and J. Yang, *Adv. Energy Mater.*, 2021, **11**, 2101494.
231 H. Zhang, X. Shen, E. Kim, M. Wang, J.-H. Lee, H. Chen, G. Zhang and J.-K. Kim, *Adv. Funct. Mater.*, 2022, **32**, 2111794.
232 P. Comanns, C. Effertz, F. Hischen, K. Staudt, W. Böhme and W. Baumgartner, *Beilstein J. Nanotechnol.*, 2011, **2**, 204–214.
233 P. Comanns, G. Buchberger, A. Buchsbaum, R. Baumgartner, A. Kogler, S. Bauer and W. Baumgartner, *J. R. Soc., Interface*, 2015, **12**, 20150415.
234 C. Dawson, J. F. Vincent, G. Jeronimidis, G. Rice and P. Forshaw, *J. Theor. Biol.*, 1999, **199**, 291–295.
235 S. Shi, B. Qian, X. Wu, H. Sun, H. Wang, H. B. Zhang, Z. Z. Yu and T. P. Russell, *Angew. Chem., Int. Ed.*, 2019, **58**, 18171–18176.
236 T. Tu, B. Liang, S. Zhang, T. Li, B. Zhang, S. Xu, X. Mao, Y. Cai, L. Fang and X. Ye, *Adv. Funct. Mater.*, 2021, **31**, 2101374.
237 M. Ashton, J. Paul, S. B. Sinnott and R. G. Hennig, *Phys. Rev. Lett.*, 2017, **118**, 106101.
238 S. Zhang, L. Wang, Y. Zeng, Y. Xu, Y. Tang, S. Luo, Y. Liu and C. Liu, *ChemCatChem*, 2016, **8**, 2557–2564.
239 N. R. Nirala, S. Pandey, A. Bansal, V. K. Singh, B. Mukherjee, P. S. Saxena and A. Srivastava, *Biosens. Bioelectron.*, 2015, **74**, 207–213.
240 P. Singh, R. P. Ojha, S. Kumar, A. K. Singh and R. Prakash, *Mater. Chem. Phys.*, 2021, **267**, 124684.
241 Z. Qu, C.-a Xu, X. Li, Y. Wu, K. Wang, X. Zheng, X. Cui, X. Wu, J. Shi and K. Wu, *Chem. Eng. J.*, 2021, **426**, 130717.
242 X. Hou, Z. Wang, G. Fan, H. Ji, S. Yi, T. Li, Y. Wang, Z. Zhang, L. Yuan, R. Zhang, J. Sun and D. Chen, *Sens. Actuators, B*, 2020, **317**, 128236.
243 J. Wang, C. Li, D. Chen, C. Sun and Z. Yang, *Appl. Surf. Sci.*, 2020, **499**, 143940.
244 X. Tang, H. Zhou, Z. Cai, D. Cheng, P. He, P. Xie, D. Zhang and T. Fan, *ACS Nano*, 2018, **12**, 3502–3511.
245 C. Androulidakis, M. Kotsidi, G. Gorgolis, C. Pavlou, L. Sygellou, G. Paterakis, N. Koutroumanis and C. Galiotis, *Sci. Rep.*, 2021, **11**, 13548.
246 F. Barati, J. P. Thompson, M. C. Dartiailh, K. Sardashti, W. Mayer, J. Yuan, K. Wickramasinghe, K. Watanabe, T. Taniguchi, H. Churchill and J. Shabani, *Nano Lett.*, 2021, **21**, 1915–1920.
247 S. H. Jo, D. H. Kang, J. Shim, J. Jeon, M. H. Jeon, G. Yoo, J. Kim, J. Lee, G. Y. Yeom, S. Lee, H. Y. Yu, C. Choi and J. H. Park, *Adv. Mater.*, 2016, **28**, 4824–4831.
248 S. R. Naqvi, G. S. Rao, W. Luo, R. Ahuja and T. Hussain, *ChemPhysChem*, 2017, **18**, 513–518.
249 D. N. Sredojević, M. R. Belić and Ž. Šljivančanin, *J. Phys. Chem. C*, 2020, **124**, 16860–16867.
250 Y. Zhang, W. Gao, Y. Li, D. Zhao and H. Yin, *RSC Adv.*, 2019, **9**, 7388–7399.
251 C. Zhi, Y. Bando, C. Tang, H. Kuwahara and D. Golberg, *Adv. Mater.*, 2009, **21**, 2889–2893.
252 J. Zhu and G. Jin, *Opt. Express*, 2022, **30**, 13469–13480.
253 M. Zhu, G. Li, W. Gong, L. Yan and X. Zhang, *Nanomicro Lett.*, 2021, **14**, 18.
254 X. Xu, Q. Zhang, M. Hao, Y. Hu, Z. Lin, L. Peng, T. Wang, X. Ren, C. Wang and Z. Zhao, *Science*, 2019, **363**, 723–727.
255 M. Q. Wu, S. Wu, Y. F. Cai, R. Z. Wang and T. X. Li, *Energy Storage Mater.*, 2021, **42**, 380–417.
256 A. Allahbakhsh and M. Arjmand, *Carbon*, 2019, **148**, 441–480.
257 D. Xu, Q. Huang, L. Yang, Y. Chen, Z. Lu, H. Liu, P. Han, L. Guo, C. Wang and C. Liu, *Carbon*, 2023, **202**, 1–12.
258 H. Liu, R. Fu, X. Su, B. Wu, H. Wang, Y. Xu and X. Liu, *Compos. Sci. Technol.*, 2021, **210**, 108835.
259 P. Goli, S. Legedza, A. Dhar, R. Salgado, J. Renteria and A. A. Balandin, *J. Power Sources*, 2014, **248**, 37–43.
260 D. Zou, X. Ma, X. Liu, P. Zheng and Y. Hu, *Int. J. Heat Mass Transfer*, 2018, **120**, 33–41.
261 S. Ye, Q. Zhang, D. Hu and J. Feng, *J. Mater. Chem. A*, 2015, **3**, 4018–4025.
262 X. Wang, G. Li, G. Hong, Q. Guo and X. Zhang, *ACS Appl. Mater. Interfaces*, 2017, **9**, 41323–41331.
263 J. Zhao, W. Luo, J.-K. Kim and J. Yang, *ACS Appl. Energy Mater.*, 2019, **2**, 3657–3664.
264 B. Mu and M. Li, *Sci. Rep.*, 2018, **8**, 1–14.
265 D. Huang, Z. Wang, X. Sheng and Y. Chen, *Sol. Energy Mater.*, 2023, **251**, 112124.
266 Y. Luo, Y. Xie, H. Jiang, Y. Chen, L. Zhang, X. Sheng, D. Xie, H. Wu and Y. Mei, *Chem. Eng. J.*, 2021, **420**, 130466.
267 P. Lin, J. Xie, Y. He, X. Lu, W. Li, J. Fang, S. Yan, L. Zhang, X. Sheng and Y. Chen, *Sol. Energy Mater.*, 2020, **206**, 110229.
268 X. Du, J. Wang, L. Jin, S. Deng, Y. Dong and S. Lin, *ACS Appl. Mater. Interfaces*, 2022, **14**, 15225–15234.
269 Z. Zheng, H. Liu, D. Wu and X. Wang, *Chem. Eng. J.*, 2022, **440**, 135862.
270 M. Amini, M. Kamkar, F. Rahmani, A. Ghaffarkhah, F. Ahmadijokani and M. Arjmand, *ACS Appl. Electron. Mater.*, 2021, **3**, 5514–5527.

271 M. Kamkar, A. Ghaffarkhah, E. Hosseini, M. Amini, S. Ghaderi and M. Arjmand, *New J. Chem.*, 2021, **45**, 21543.
272 B.-X. Li, Z. Luo, W.-G. Yang, H. Sun, Y. Ding, Z.-Z. Yu and D. Yang, *ACS Nano*, 2023, **17**, 6875–6885.
273 X. Ji, Y. Jiang, T. Liu, S. Lin and A. Du, *Cell Rep. Phys. Sci.*, 2022, **3**, 100815.
274 W. Han, C. Ge, R. Zhang, Z. Ma, L. Wang and X. Zhang, *Appl. Energy*, 2019, **238**, 942–951.
275 X. Jia, Q. Li, C. Ao, R. Hu, T. Xia, Z. Xue, Q. Wang, X. Deng, W. Zhang and C. Lu, *Composites, Part A*, 2020, **129**, 105710.
276 L. Song, L. Ci, H. Lu, P. B. Sorokin, C. Jin, J. Ni, A. G. Kvashnin, D. G. Kvashnin, J. Lou and B. I. Yakobson, *Nano Lett.*, 2010, **10**, 3209–3215.
277 J. Yang, L.-S. Tang, R.-Y. Bao, L. Bai, Z.-Y. Liu, W. Yang, B.-H. Xie and M.-B. Yang, *J. Mater. Chem. A*, 2016, **4**, 18841–18851.
278 K. Zhang, Y. Feng, F. Wang, Z. Yang and J. Wang, *J. Mater. Chem. C*, 2017, **5**, 11992–12022.
279 Y. Ma, H. Wang, L. Zhang, X. Sheng and Y. Chen, *Composites, Part A*, 2022, **163**, 107203.
280 L. Wan, C. Liu, D. Cao, X. Sun and H. Zhu, *ACS Appl. Polym. Mater.*, 2020, **2**, 3001–3009.
281 D. Liu, C. Lei, K. Wu and Q. Fu, *ACS Nano*, 2020, **14**, 15738–15747.
282 G. Du, X. Lai, J. Hu and Z. Zhang, *Sol. Energy Mater.*, 2022, **240**, 111532.
283 M. Yang, H. Dong, K. Sun, Y. Kou, L. Zhang, J. Zhao, Y. Song and Q. Shi, *J. Energy Storage*, 2022, **56**, 105954.
284 Y. Cao, D. Fan, S. Lin, F. T. T. Ng and Q. Pan, *Renew. Energy*, 2021, **179**, 687–695.
285 Q. Guo, H. Yi, F. Jia and S. Song, *Desalination*, 2022, **541**, 116028.
286 Y. Zhang, C. Ma, J. Xie, H. Ågren and H. Zhang, *Adv. Mater.*, 2021, **33**, 2100113.
287 Z. Zheng, T. Shi, H. Liu, D. Wu and X. Wang, *Appl. Therm. Eng.*, 2022, 118173.
288 W. Ren, L. Cao and D. Zhang, *Int. J. Energy Res.*, 2020, **44**, 242–256.
289 P. Min, J. Liu, X. Li, F. An, P. Liu, Y. Shen, N. Koratkar and Z. Z. Yu, *Adv. Funct. Mater.*, 2018, **28**, 1805365.
290 G. Chen, Y. Su, D. Jiang, L. Pan and S. Li, *Appl. Energy*, 2020, **264**, 114786.
291 Q. Cao, F. He, C. Xie, J. Fan, J. Wu, K. Zhang, Z. Yang and W. Yang, *Fuller. Nanotub.*, 2019, **27**, 492–497.
292 Y. Xia, W. Cui, H. Zhang, F. Xu, L. Sun, Y. Zou, H. Chu and E. Yan, *J. Mater. Chem. A*, 2017, **5**, 15191–15199.
293 J. Yang, G.-Q. Qi, Y. Liu, R.-Y. Bao, Z.-Y. Liu, W. Yang, B.-H. Xie and M.-B. Yang, *Carbon*, 2016, **100**, 693–702.
294 Q. Cao, F. He, Y. Li, Z. He, J. Fan, R. Wang, W. Hu, K. Zhang and W. Yang, *Fuller. Nanotub.*, 2020, **28**, 656–662.
295 D. Wei, C. Wu, G. Jiang, X. Sheng and Y. Xie, *Sol. Energy Mater.*, 2021, **224**, 111013.
296 J. Qiu, X. Fan, Y. Shi, S. Zhang, X. Jin, W. Wang and B. Tang, *J. Mater. Chem. A*, 2019, **7**, 21371–21377.
297 P. Liu, F. An, X. Lu, X. Li, P. Min, C. Shu, W. Li and Z.-Z. Yu, *Compos. Sci. Technol.*, 2021, **201**, 108492.
298 J. Yang, X. Li, S. Han, Y. Zhang, P. Min, N. Koratkar and Z.-Z. Yu, *J. Mater. Chem. A*, 2016, **4**, 18067–18074.
299 B. Mu and M. Li, *Sol. Energy Mater.*, 2019, **191**, 466–475.
300 F. Xue, X.-Z. Jin, W.-Y. Wang, X.-D. Qi, J.-H. Yang and Y. Wang, *Nanoscale*, 2020, **12**, 4005–4017.
301 S. Xi, M. Wang, L. Wang, H. Xie and W. Yu, *Sol. Energy Mater.*, 2021, **226**, 111068.
302 J. Yang, G.-Q. Qi, R.-Y. Bao, K. Yi, M. Li, L. Peng, Z. Cai, M.-B. Yang, D. Wei and W. Yang, *Energy Storage Mater.*, 2018, **13**, 88–95.
303 X. Zheng, X. Gao, Z. Huang, Z. Li, Y. Fang and Z. Zhang, *Sol. Energy Mater.*, 2021, **226**, 111083.
304 X. Du, M. Zhou, S. Deng, Z. Du, X. Cheng and H. Wang, *Cellulose*, 2020, **27**, 4679–4690.
305 R. Cao, D. Sun, L. Wang, Z. Yan, W. Liu, X. Wang and X. Zhang, *J. Mater. Chem. A*, 2020, **8**, 13207–13217.
306 C. Yu, H. Kim, J. R. Youn and Y. S. Song, *ACS Appl. Energy Mater.*, 2021, **4**, 11666–11674.
307 C. Yu, S. H. Yang, S. Y. Pak, J. R. Youn and Y. S. Song, *Energy Convers. Manage.*, 2018, **169**, 88–96.
308 S. Xi, L. Wang, H. Xie and W. Yu, *ACS Nano*, 2022, **16**, 3843–3851.
309 H. Ai, L. Lv, T. Chen, Y. Zhang, L. Dong and S. Song, *Energy Convers. Manage.*, 2022, **253**, 115172.
310 Y. Xu, A. S. Fleischer and G. Feng, *Carbon*, 2017, **114**, 334–346.
311 J. Yang, E. Zhang, X. Li, Y. Zhang, J. Qu and Z.-Z. Yu, *Carbon*, 2016, **98**, 50–57.
312 M. Wang, T. Zhang, D. Mao, Y. Yao, X. Zeng, L. Ren, Q. Cai, S. Mateti, L. H. Li and X. Zeng, *ACS Nano*, 2019, **13**, 7402–7409.
313 K. Wang and R. Wen, *J. Energy Storage*, 2023, **58**, 106302.
314 B. Tian, W. Yang, F. He, C. Xie, K. Zhang, J. Fan and J. Wu, *Fuller. Nanotub.*, 2017, **25**, 512–518.
315 J. Huang, B. Zhang, M. He, X. Huang, G. Wu, G. Yin and Y. Cui, *J. Mater. Sci.*, 2020, **55**, 7337–7350.
316 J. Feng, X. Liu, F. Lin, S. Duan, K. Zeng, Y. Bai, X. Wu, Z. Huang and X. Min, *Carbon*, 2023, **201**, 756–764.
317 M. Guo, P. Xu, J. Lv, C. Gong, Z. Zhang and C. Li, *Diamond Relat. Mater.*, 2022, **127**, 109131.
318 F. Xue, X.-Z. Jin, X. Xie, X.-D. Qi, J.-H. Yang and Y. Wang, *Nanoscale*, 2019, **11**, 18691–18701.
319 X. Liu, F. Lin, X. Zhang, M. Liu, Z. Sun, L. Zhang, X. Min, R. Mi and Z. Huang, *Energy Fuels*, 2021, **35**, 2805–2814.
320 L. Tang, X. Zhao, C. Feng, L. Bai, J. Yang, R. Bao, Z. Liu, M. Yang and W. Yang, *Sol. Energy Mater.*, 2019, **203**, 110174.
321 Z. Cheng, G. Chang, B. Xue, L. Xie and Q. Zheng, *J. Mater. Sci. Technol.*, 2023, **132**, 132–143.
322 X.-Z. Jin, Z.-Y. Yang, C.-H. Huang, J.-H. Yang and Y. Wang, *Chem. Eng. J.*, 2022, **448**, 137599.
323 C. Lei, K. Wu, L. Wu, W. Liu, R. Du, F. Chen and Q. Fu, *J. Mater. Chem. A*, 2019, **7**, 19364–19373.
324 G. Yang, B. Wang, H. Cheng, Z. Mao, H. Xu, Y. Zhong, X. Feng, J. Yu and X. Sui, *Int. J. Biol. Macromol.*, 2020, **148**, 627–634.
325 Y. Wei, J. Li, F. Sun, J. Wu and L. Zhao, *Green Chem.*, 2018, **20**, 1858–1865.
326 F. Cao, Y. Zhang, H. Wang, K. Khan, A. K. Tareen, W. Qian, H. Zhang and H. Ågren, *Adv. Mater.*, 2022, **34**, 2107554.